

X-ray Mass Estimates at $z \sim 0.3$ for the CNOC Cluster Sample

Aaron D. Lewis¹ and E. Ellingson²

Center for Astrophysics and Space Astronomy,
University of Colorado at Boulder, Campus Box 389, Boulder, CO, 80309

Simon L. Morris³

National Research Council of Canada, Herzberg Institute of Astrophysics, Dominion
Astrophysical Observatory, 5071 West Saanich Road, Victoria, B.C., V8X 4M6, Canada

and

R. G. Carlberg⁴

Department of Astronomy, University of Toronto, Toronto, Ontario, M5S 1A7 Canada

ABSTRACT

Results are presented from the analysis of ROSAT HRI and PSPC observations of the CNOC subsample of the EMSS high redshift galaxy clusters. X-ray surface brightness profiles of 14 clusters with $0.17 < z < 0.55$ are constructed and fit to isothermal β models. Where possible, we use both the HRI and PSPC data to constrain the fit. Under the assumptions of isothermality, hydrostatic equilibrium, and spherical symmetry, we derive total X-ray masses within a range of radii from 141 to $526h_{100}^{-1}$ kpc. These masses are compared with both the dynamical masses obtained from galaxy velocities and the projected masses from published gravitational lensing studies. We find no systematic bias between X-ray and dynamical methods across the sample, with an average $M_{Dym}/M_X = 1.04 \pm 0.07$, although individual clusters exhibit mass discrepancies up to a factor of 2. We estimate that the systematic effects due to cooling flows, non-equilibrium systems and temperature gradients affect the average mass ratio by no more than 15 – 20%. Weak gravitational lensing masses appear to be systematically higher than X-ray results by factors of $\sim 50\%$, while strong lensing estimates show larger

¹lewisad@colorado.edu

²e.elling@casa.colorado.edu

³Simon.Morris@hia.nrc.ca

⁴carlberg@moonray.astro.utoronto.ca

discrepancies (factors of ~ 2.5). However, these comparisons are complicated by the need to extrapolate the X-ray data to larger or smaller radii. X-ray derived cluster gas masses are calculated, from which we obtain a cluster baryon fraction of $\sim 5\%h_{100}^{-3/2}$, yielding $\Omega_0 \sim 0.3h_{100}^{-1/2}$.

Subject headings: cosmology:observations — X-rays:galaxies — galaxies:clusters:general — gravitational lensing

1. Introduction

Clusters of galaxies are the largest gravitationally bound systems in the universe, and hence serve as critical regions for cosmological studies. This has led to their extensive use as a probe of the evolution of large scale structure (see Henry 1997 for a review). Of particular interest to cosmologists, clusters may directly constrain the universal density parameter, Ω . Under the assumption that the co-moving volume from which the cluster formed contains the same fraction of baryons and dark matter as the field, cluster mass-to-light ratios or cluster baryon fractions yield a value of Ω (the latter method also requires a value of Ω_b , White et al. 1993; Carlberg et al. 1996, C96 hereafter; Sadat, Blanchard, & Oukbir 1997).

Additionally, measurements that constrain the evolution of the cluster luminosity function and mass function are basic to our understanding of large scale structure in the universe (c.f. Oukbir & Blanchard 1997), as well as providing the observational data necessary to constrain theoretical models of structure formation (Henry 1997). The accurate determination of both total gravitational cluster masses and the mass of baryonic matter in clusters is thus crucial to cosmology.

Intermediate redshift ($0.2 \lesssim z \lesssim 0.6$) clusters are optimal for the study of cluster properties. They are ubiquitous enough to be found in statistically useful numbers, they are compact enough to be observed in a single field of view with modern instrumentation, and they are bright enough to permit detailed investigation. The hot (10^8 K), diffuse (10^{-3} cm $^{-3}$) intracluster medium (ICM) may be the most accurate tracer of the potential well of the cluster. Following the assumptions of hydrostatic equilibrium and isothermality, the surface brightness distribution of a resolved X-ray image yields the ICM density as well as the cluster mass (Cavaliere & Fusco-Femiano 1976; Bahcall & Sarazin 1977). The longevity of the ROSAT and ASCA satellites has allowed us to compile long pointed exposures of a sample of clusters at intermediate redshift, to obtain a statistical comparison of mass determination methods.

Additional methods for cluster mass determinations include the optical measurement of galaxy redshifts with subsequent virial/dynamical analysis, and the measurement of both weak and strong gravitational lensing of background galaxies by the cluster mass potential. Theoretically, all three methods should accurately provide the same results, yet there have been discrepancies reported among the techniques (e.g. Carlberg, Yee, & Ellingson 1994; Fahlman et al. 1994; Miralde-Escudé & Babul 1995; Wu & Fang 1997, WF97 hereafter; Allen 1998, A98 hereafter; Wu et al. 1998, W98 hereafter). Each method is subject to possible systematic errors. Our goal is to analyze a well-defined sample of clusters and identify any discrepancies between the three methods, including any systematic biases. Therefore we have performed an X-ray analysis of a sample of 14 clusters which have been observed optically and have a detailed dynamical/virial analysis. In addition, many of the clusters have gravitational lens measurements published for comparison.

In §2 we describe the cluster sample and the data. We present the data reduction methods in §3. Analysis of the data is in §4, with discussion in §5, and conclusions in §6. The Appendix contains notes on individual clusters and their analysis.

This paper assumes $H_0 = 100h \text{ km s}^{-1} \text{ Mpc}^{-1}$ and $q_0 = 0.1$ unless otherwise noted.

2. Cluster Sample & Data

We have chosen to analyze the available X-ray data on clusters within the CNOC (Canadian Network for Observational Cosmology, Yee, Ellingson, & Carlberg 1996) intermediate redshift subsample of 15 EMSS (Extended Medium Sensitivity Survey) distant clusters (Gioia et al. 1990; Henry et al. 1992). The CNOC sample also includes the optically selected cluster Abell 2390, another rich, X-ray luminous cluster. Spectroscopic observations were performed at the CFHT 3.6 m telescope at Mauna Kea by the CNOC collaboration, who obtained 30-200 galaxy velocities per cluster, as well as accurate photometry. For a discussion of the selection criterion for this sample, see Yee et al. (1996). The dynamical analyses of these data are presented in C96 and Carlberg et al. (1997).

Here we present an analysis of the available ROSAT X-ray observations of this sample. To resolve the X-ray core structures of clusters at these redshifts, the $\sim 5''$ FWHM resolution of the High Resolution Imager (HRI) is necessary. At a redshift of 0.3, $5'' \simeq 15h^{-1} \text{ kpc}$. Thus the $\sim 30''$ FWHM of the ROSAT Position Sensitive Proportional Counter (PSPC) cannot resolve structure smaller than $\sim 90h^{-1} \text{ kpc}$, making its use problematic with clusters with small core radii.

The HRI is a mature instrument, and all 16 of the CNOC clusters have been the sub-

ject of pointed observations by us and other investigators. Two of the CNOC clusters, MS 1231.3+1542 and MS 1621.5+2640, have HRI observations which do not allow us to extract adequate surface brightness profiles, and are not discussed in this work. We present here results from the 14 remaining clusters in the CNOC sample. These HRI images comprise the primary data sets for our analysis.

In addition, we have analyzed ROSAT PSPC images of 5 of the CNOC clusters from the public archives. Additional serendipitous PSPC observations of MS 1231.3+1542 and MS 1512.4+3647 are available, but are of insufficient duration for our analysis. A combined analysis of the two data sets, where available, is utilized to yield a more accurate model of the X-ray surface brightness profiles. Table 1 lists the clusters in the sample with their identification, redshift, and L_x in the *Einstein* IPC band, in columns (1), (2), and (3), respectively. Columns (4) and (5) list the total duration of the HRI and PSPC observations used in our analysis, respectively.

3. Data Reduction

3.1. HRI data sets

We use the IRAF/PROS⁵, STSDAS⁶, and ESAS⁷ analysis packages to reduce the data. Each observation is inspected for periods of unacceptably high count rates, which are primarily due to cosmic ray events or pointing of the spacecraft too close to the Earth or Sun. Standard pipeline analysis by the ROSAT data facility succeeds in eliminating nearly all such events. The majority of each data set consists of 0.5 – 2 ksec blocks of continuous pointed observation. We eliminate any block under 50 s to avoid periods of unstable or unreliable pointing and peculiar timing effects. After time filtering, multiple observations

⁵The Image Reduction and Analysis Facility (IRAF) is distributed by the National Optical Astronomy Observatories, which is operated by the Association of Universities for Research in Astronomy, Inc. (AURA), under contract to the National Science Foundation. The Post Reduction Off-line Software (PROS) package was developed by the High Energy Astrophysics Division of the Smithsonian Astrophysical Observatory, with assistance from the Space Science Computing Division and the Laboratory for High Energy Astrophysics of the Goddard Space Flight Center.

⁶The Space Telescope Science Data Analysis Software Package (STSDAS) software is distributed by the Space Telescope Science Institute (STScI) software development group. STScI is operated by AURA for the National Aeronautics and Space Administration.

⁷The Extended Source Analysis Software (ESAS) package created by Steve Snowden (Snowden et al. 1995) is available at the ROSAT GOF, <ftp://legacy.gsfc.nasa.gov/rosat/software/fortran/sxrb/>

of the same cluster are combined, and the resulting data set is checked to ensure accurate mapping of sky coordinates, as some observations are performed months or years apart.

The HRI has a pixel scale of $0.5'' \text{ pixel}^{-1}$, and the instrument efficiency within a radius of $5'$ varies by less than 10% ⁸ (partly owing to the intentional ‘wobble’ of the spacecraft during each observation). For all of our clusters, the detected cluster emission does not extend beyond this region. However, to include a large enough area to allow background measurements, we perform our analysis over a region 700 pixels in radius. Thus we employ the ESAS software to create exposure and particle background maps that take into account time, energy and pixel-to-pixel variation in the detector during the observation. Images of each cluster (with X-ray surface brightness contours overlaid to emphasize structure) are presented in Figure 1. The X-ray center of each cluster is identified by iteratively fitting a two dimensional 5 pixel FWHM gaussian to a blocked (by a factor of 8), smoothed (with a gaussian of 1 pixel FWHM), particle-background and exposure corrected image to find the highest peak. Cluster centers generally coincide within $1''$ of the brightest pixel on the X-ray image, and within $5''$ of the brightest cluster galaxy (BCG) identified optically (c.f. Gioia & Luppino 1994, see the Appendix for a discussion of individual offsets). Point sources are similarly identified, and their positions and extent are recorded in an image mask, which is later used to avoid contamination of the surface brightness profile, or the flux calculation (see §4).

3.2. PSPC data sets

The PSPC has time, energy, and pixel dependent variations of the instrument efficiency and the detector resolution which are much greater than those affecting the HRI. Accurate exposure, background, and scattered solar X-ray maps in each energy band must be used to properly recover the signal in an image. We have used the ESAS package to create images which are corrected for these effects. We restrict our analysis to the PSPC bands R4 through R7, also known as SASS band B, corresponding to an observed energy band of $0.44 - 2.04 \text{ keV}$. We identify cluster centers and any point sources in a similar fashion to the HRI reduction.

4. Data Analysis

⁸Details may be found in “The ROSAT High Resolution Imager (HRI) Calibration Report”, available at <http://hea-www.harvard.edu/rosat/rsdc-www/HTI-CAL-REPORT/hri.html>

4.1. Surface Brightness Profiles

After the initial reduction described in the previous section, each image is binned into radial annuli about the cluster center (165 annuli for HRI data, 50 for PSPC) out to a maximum radius (700 pixels for HRI, 50 for PSPC), and a radial surface brightness profile is constructed by summing the counts in each bin.

In some cases, the X-ray emission is detectably elliptical or irregular. In the former case a more acceptable fit may be found using elliptical, rather than radial, surface brightness profiles. However, the use of elliptical coordinates is problematic, in that the position angle of elliptical isophotes changes with increasing radius introducing an additional free parameter to the fit, which can be difficult to constrain with statistical significance for our noisier datasets. As discussed in Neumann & Böhringer (1997) and Böhringer et al. (1998), the difference in the derived mass caused by an ellipticity such as that evident in Abell 2390 is less than 5 percent compared with that derived from a radially symmetric profile. We note that in the case of MS 0015.9+1609, which exhibits significant non-circularity, a radial and elliptical analysis has been performed by Neumann & Böhringer (1997), and the fitted β parameters, and hence the masses, for the two models are identical. We have chosen to use radial profiles throughout this work for simplicity, consistency in analysis between clusters, and for our comparison with the dynamical masses (which also assume sphericity). Other uncertainties in the analysis (e.g. in the temperature) dominate any error introduced by assuming radial symmetry.

The projected radial surface brightness profile is then fit via a non-linear least squares routine to a standard isothermal β -model (Cavaliere & Fusco-Femiano 1976; Bahcall & Sarazin 1977)

$$S(b) = S_0[1 + (b/r_{core})^2]^{-3\beta+1/2} + C, \quad (1)$$

where S_0 is the central surface brightness, r_{core} is the cluster core radius, β is the ratio of energy per unit mass in the galaxies to that in the gas, and C is the background. Note that we fit a uniform background assumed to be cosmic in origin, which is in addition to the particle background we have derived with the ESAS software and previously subtracted.

As has been noted by several authors (e.g. Jones & Forman 1984), an isothermal β model is inaccurate for clusters out of equilibrium (e.g. undergoing a merger or sub-merger), or those with large temperature gradients. Clusters in our sample in general exhibit regular X-ray and optical morphology and galaxy velocity distributions, although a few of the clusters do show signs of recent merging activity. We discuss these and other possible effects on our results in §5.

Based on either narrow-band optical or X-ray images, several clusters have been identi-

fied or are candidates for large central cooling flows (c.f. Donahue, Stocke, & Gioia 1992, D92 hereafter; Pierre et al. 1996; Allen et al. 1996; Rizza et al. 1997), in some cases accounting for 25% of the total observed X-ray luminosity. In an X-ray image, a cooling flow may be expected to be seen as a sharp peak in emission concentrated in the core of a cluster, where the cooling time for the ICM is shorter than the current age of the universe at the cluster redshift.

One problem introduced by a cooling flow is its effect on our attempt to fit a β model to the observed surface brightness profile. If a cooling flow is present in the cluster one would expect to see an uncharacteristically high central peak in the radial profile, or a second shoulder at smaller radius than the shoulder related to the r_{core} parameter. If the shoulder of the cooling flow is indistinguishable from the underlying profile, it will result in a lower fitted value of the r_{core} parameter. Unfortunately, uncertainties in the fit to the r_{core} parameter are directly correlated with those in the β parameter, and a low fitted value of r_{core} will result in a low fitted β value.

To partially avoid the problems of lower fitted r_{core} and hence lower fitted β values, we have attempted to eliminate the effect of any peaked cooling flow emission from the fit. In appropriate cases, we have used a method similar to the pioneering work of Jones & Forman (1984) who excluded central regions of clusters with excess emission, in order to obtain an acceptable fit. We subjectively identified an inner cutoff radius based on a significant increase in emission at a radius smaller than the obvious shoulder of the profile, and excluded data within that radius from the least-squares fit to the β model. In some cases, the cutoff radius is not obvious, although a cooling flow may still be present. In Figure 2 we present the HRI surface brightness profiles, overlaid with best fit β models when all points are included in the fit (solid line) and only points outside the chosen cutoff radius are included (dotted line). The inner cutoff radius, where applicable, is indicated in Figure 2 with a vertical dashed-dotted line.

Observations at other wavelengths may also imply a cooling flow, for instance $H\alpha$ filaments (Heckman et al. 1989), or emission line signatures in the spectra of the brightest cluster galaxy (BCG). Based on the observed [O II] emission from the CNOC observations (Balogh et al. 1997) and a study of extended $H\alpha$ in EMSS clusters by D92 we have attempted to identify the existence and estimate the strength of a possible cooling flow in each cluster. We found that [O II] emission in our BCG spectra is not well correlated with apparent cooling flow size. However, all large cooling flows in the sample had significant [O II] emission, and non-cooling flow clusters did not. Thus, the presence of [O II] emission in the galaxy spectra can be regarded as an indicator of possible cooling, though not a reliable measure of the strength of the cooling flow.

D92 detected extended $H\alpha$ emission on scales of tens of kpc for several clusters in our sample. In Figure 3 we have plotted the ratio of $H\alpha$ /X-ray luminosity versus the inner cutoff radius. We choose the ratio of luminosities to account for the fact that a cooling flow of a given $H\alpha$ luminosity will have a greater perturbation on the profile of a poor cluster than on a rich one. There appears to be a mild correlation between this ratio and the empirical inner cutoff radius described above. However, we do not feel this correlation should be used to estimate the cooling radius in lieu of inspection of a surface brightness profile; rather we regard the correlation as an independent justification for our identification of which clusters have significant cooling flows, and our subjective choice of cutoff radius.

High spatial resolution is important to constrain both r_{core} (especially at these redshifts), and the effects of cooling flows, while low background counts are needed for a more accurate measurement of the faint slope in the tail of the surface brightness distribution, which constrains β . As discussed in Rizza et al. (1997), HRI observations may not allow an accurate measurement of the slope of the tail of the cluster profile, due to the high background of the instrument. The slope of the surface brightness profile is the primary constraint on the fit to the β parameter, and a high and irregular background may mask out the signal of an increasing slope, resulting in a fit to a flattened slope and correspondingly low fitted β value. Even if we have minimized the effect of a cooling flow on the β -model fits, we are still faced with the high background of the HRI. To improve our fits, we have utilized PSPC data where available. The PSPC data are in general not sufficient to resolve the cores of the clusters. However, they do provide a lower background count rate, allowing cluster surface brightness profiles to be accurately measured to greater radii than with HRI data alone. We attempted use a combined profile to more accurately describe the true shape of the cluster emission than would be possible with a single instrument. First we constrain the r_{core} parameter with the HRI data, and then use it as a fixed value when fitting to the PSPC data, from which we derive final β values. In cases where we excluded inner regions from the HRI fit to avoid cooling emission, we also excluded the same region from the subsequent PSPC fit. Parameter values from the HRI, PSPC, and the combined data sets are shown in Table 2, columns (2) & (3), (4) & (5), and (6) & (7), respectively. In this way, we hope to most effectively utilize the strengths of each instrument. We note that the PSPC fits obtained solely with PSPC data (independent of the HRI r_{core} value) are in general agreement with the HRI’s independent fits (see the Appendix for individual cases).

5. Discussion

5.1. Cluster Mass Determinations

Under the assumption of an isothermal sphere in hydrostatic equilibrium (Sarazin 1988), where the gas and the dark matter are identically distributed, we can calculate the total X-ray derived gravitational mass within a radius r

$$M_X(< r) = 1.13 \times 10^{15} \beta \left[\frac{T}{10 \text{keV}} \right] \left[\frac{r}{\text{Mpc}} \right] \frac{(r/r_{\text{core}})^2}{(1 + (r/r_{\text{core}})^2)} h^{-1} \text{M}_{\odot}, \quad (2)$$

where T is the isothermal gas temperature. The parameters β and r_{core} were obtained as described in the previous section. The cluster temperatures are listed in Table 2, column (8). The majority have been obtained from pointed ASCA observations of each cluster analyzed by Mushotzky & Scharf (1997). For MS 0906.5+1110 we use the L_x – T_x relationship from Mushotzky & Scharf (1997) to estimate the gas temperature because no direct measurement is available. The uncertainty in the temperature is estimated from the scatter in the relation.

For MS 0302.7+1658 and MS 1006.0+1202 we use the empirical Bgc- T_x relation. The quantity Bgc is a statistical measure of the galaxy overdensity within the cluster (c.f. Yee & Green 1987). This quantity is well-correlated with both the velocity dispersion and T_x for these clusters (see also Yee & Lopez-Cruz 1998). Since it is based purely on the photometry of galaxies in the cluster, it is essentially an independent estimate of the cluster richness; which, unlike L_x , is not affected by cooling flows. Uncertainty in the temperature values are estimated from the scatter in the Bgc- T_x relation (Yee et al. 1999).

Table 3 lists the inner cutoff radius for each cluster (column 2), the cluster radius where the HRI signal drops to 2σ above the noise (column 3), and the total X-ray derived mass within this radius (column 4). We have plotted the total mass profiles for each cluster in Figure 4 (solid curves). Also listed in Table 3 are the 2σ outer cutoff radii for the PSPC data and the masses within these radii (columns 6 & 7, respectively). Uncertainties in the masses are 1σ statistical errors associated with the β model parameters and the temperatures.

Of primary interest is a comparison of total cluster mass estimates from this method with both dynamical/virial analyses and gravitational lensing techniques. Many authors have reported lensing masses in excess of the results of other techniques (e.g. Fahlman et al. 1994; Miralde-Escudé & Babul 1995). WF97 find good agreement between dynamical and lensing methods for a large sample including eight of the CNOC clusters; however they report X-ray calculated masses a factor of 2-3 lower than lensing mass estimates. A98 performed a detailed analysis of a nearly identical subsample of the clusters analyzed by WF97, including a cooling flow analysis, concluding that strong lensing and X-ray mass estimates are in good agreement for strong cooling flow clusters, which they identify as the only truly relaxed systems.

We have included in Table 3 a mass comparison between the X-ray and the dynamical/virial methods (our comparison with gravitational lensing is discussed in §5.3). Virial mass estimates for each cluster are taken from C96, and scaled to our 2σ cutoff radius according to the observed galaxy density distribution, which Carlberg et al. (1997) found to be well-fit by a Navarro profile (Navarro, Frenk, & White 1996) of the form:

$$\rho_{gal}(r') = \frac{\rho_0}{(r/r_{200})(0.27 + r/r_{200})^2} \quad (3)$$

where r_{200} is the radius at which the cluster density is 200 times the critical density, as tabulated in Carlberg, Yee, & Ellingson (1997, C97 hereafter), and r' is simply equal to (r/r_{200}) . The total dynamically derived gravitational mass enclosed within a radius r is then given by:

$$M_{Dyn}(< r) = \frac{0.82 h^{-1} M_{200}}{9.56} \int_0^r 4\pi(r')^2 \rho(r') dr' \quad (4)$$

where the factor of 0.82 ± 0.14 is an empirically derived correction by C97 to the virial mass estimate based on the more detailed dynamical mass estimate, and M_{200} is the total mass enclosed at r_{200} (also tabulated in C97). The factor of 9.56 is the normalization of equation 4 required to yield $M = M_{200}$ at $r = r_{200}$. Note that our cosmology has been chosen to match that of C96, so that the masses may be directly compared.

We have overlaid the dynamical mass profiles on the X-ray derived mass profiles in Figure 4 (dashed curves). Note that the basic shapes of the profiles are similar due to the inherent similarity between a Navarro density profile and an isothermal β -model density profile; however the normalization and shoulders of the profiles are constrained by independently determined parameters. Across the sample, clusters exhibit a scatter of both higher and lower X-ray masses relative to the dynamical masses. In Table 3, column (5), we have listed the ratio of dynamically to X-ray derived mass for each cluster at the HRI 2σ cutoff radii. These mass ratios are also plotted in Figures 5 and 6 as functions of cluster mass and the 2σ radius, respectively. Note that we have omitted MS 0906.5+1110 from the dynamical/X-ray comparison; its spuriously high velocity dispersion invalidates the dynamical mass calculation (C96). In addition, we have increased the uncertainty associated with the velocity dispersion for MS 0440.5+0204 to include a recent measurement made by Gioia et al. (1998).

We find that the masses from the dynamical and X-ray methods have a weighted average ratio of 1.04 ± 0.07 with an rms scatter in the individual points of 0.27. Statistically, the dynamical/X-ray mass ratios (M_{Dyn}/M_X ratios, hereafter) show no intrinsic scatter above the $\sim 20 - 30\%$ observational uncertainties. However, our pre-selection of rich, X-ray luminous systems, and especially our exclusion of the probable merging cluster MS 0906.5+1110 (see

below), undoubtedly plays a role in producing the relatively small scatter in Figures 5 and 6. C96 also found a small scatter in the distribution of dynamical M/L ratios for these clusters, a further indication of the relative uniformity of the sample.

We have analyzed the data in Figure 5 to determine if there is a correlation between the M_{Dym}/M_X ratio and the cluster mass. There appears to be a slight systematic gradient, with lower masses having slightly lower ratios. We fit the data points with both a zero slope line and with a free parameter for the slope. The addition of the slope parameter is only significant at the 1.5σ level and the range of differences over our sample is about 10%, similar to the uncertainty in the mean value. We note that the correlation becomes somewhat weaker if plotted as a function of the radius at which the mass measurement is made (see Figure 6). This suggests that if the correlation with mass is real, it may be due to small systematic differences in cluster properties as a function of their mass, rather than observational effects. A larger sample will be necessary to confirm whether this gradient is indeed statistically significant.

5.2. Systematic Biases in the X-ray Mass Estimates

The agreement between the independent X-ray and dynamical cluster mass estimates is good, implying that these cluster mass estimates are unbiased to within $\sim 10\%$ systematic uncertainty. However, a number of possible systematic errors in the X-ray mass estimates must still be addressed. The effects of the instrumental point spread function (PSF), large-scale temperature gradients, cooling flows, and cluster substructure may all contribute unaccounted-for biases in the X-ray masses. While the agreement between the two independent methods is greatly encouraging, the magnitude of these effects must be estimated in order to place a firm limit on the maximum possible bias in the cluster mass estimates.

5.2.1. Instrumental PSF

First we address the effect of the instrumental PSF on the data. For those clusters with the smallest core radii, the $5''$ HRI PSF may increase the fitted r_{core} value (and the fitted β value). To obtain a first-order estimate of the effect of the PSF, we simulate cluster data with various core radii and convolve them with a gaussian of FWHM comparable to the HRI PSF ($\sim 5''$). Fitting these data with β -models allows us to estimate the increase in parameters due to the PSF. For the cluster with the smallest measured core radii (MS 1512.4+3647

with $r_{core} = 9''$), we estimate a systematic increase of $\sim 46\%$ in r_{core} and $\sim 6\%$ in β due to the HRI PSF. For the next smallest cluster core (MS 0302.7+1658 with $r_{core} = 10''$), the estimated increase is $\sim 24\%$ in r_{core} and $\sim 6\%$ in β . Continuing to larger core radii, for MS 1455.0+2232 the effect of the PSF is to increase r_{core} by $\sim 16\%$ and β by $\sim 4\%$. For the remaining clusters, the net effect is no greater than $\sim 9\%$ for the r_{core} parameter, and $\sim 2\%$ for the β parameter.

Since the resolution of the PSPC is comparable to or greater than the core radii in our sample, we do not use it to measure the core radii, but instead adopt the HRI values for our iterative fits. We used a similar method as that described above for the HRI to estimate the effects of the PSPC PSF on β . For the MS 1358.4+6245 PSPC data, the final fitted β value is changed by 8% due to broadening by the PSF; all other clusters are affected by less than 5%.

Although the HRI PSF can increase the fitted value for r_{core} , and decrease the value of β , the net effect on the X-ray masses are actually quite small. This is partly because we calculate the enclosed mass at many core radii, but also because the effects on the two parameters tend to partially cancel. If we correct the final fitted values for the cluster sample to account for the PSF of both instruments, the greatest effect on any of our X-ray derived mass estimates is to decrease it by 6% (in the case of MS 1512.4+3647). Three other clusters exhibit a decrease of 3%, and the remaining clusters change less than 2%. The overall affect on the weighted average M_{Dyn}/M_X ratio for the sample is negligible. Applying corrections for the PSF, the weighted average ratio for the entire cluster sample is increased by 0.2%. On a subsample of 9 clusters identified as cooling flow clusters (see below), the weighted average is decreased by 0.4%. In both cases this correction is many times smaller than other possible sources of bias. Thus we choose to present uncorrected values in all tables and figures.

5.2.2. Large-Scale Temperature Gradients

As mentioned in §3, our assumption of isothermality may not always be valid. Clusters of galaxies often show evidence for substructure in their X-ray emission and their distribution of galaxies, both of which could be signatures of non-isothermality. However, the clusters in this sample include some of the richest and most relaxed systems known. We will attempt to quantify below the effect that a reasonable temperature gradient might have for such systems. We do not expect extreme temperature gradients due to the short equilibration timescale of the intracluster gas (David, Jones & Forman 1996).

Recently, Markevitch et al. (1998) used extensive ASCA observations to construct tem-

perature profiles for 30 nearby ($z \sim 0.05$) clusters. They observed a similarity among all the profiles, with decreasing temperature at larger radii. Assuming a uniform temperature gradient comparable to that found for their sample, we can estimate the effect of large-scale temperature gradients on our mass estimates. We approximate the temperature gradient as a power law across the range of radii at which we measure cluster masses, and assume the following form:

$$\frac{T(r)}{T_0} = A \left(\frac{r}{r_{180}} \right)^{-\alpha} \quad (5)$$

where T_0 is the emission-weighted temperature we have previously assumed, r_{180} is the cluster radius at which the density equals 180 times the critical density, and α and A are constants. If a mass density $\propto r^{-2}$ is assumed, r_{180} equals $1.054 r_{200}$. A non-isothermal temperature requires inclusion of a second term in the X-ray mass calculation that accounts for the temperature gradient. After replacing the emission-weighted temperature with the assumed power-law temperature form, we obtain a new X-ray estimate for the total cluster mass:

$$M_{X_{grad}}(< r) = M_{X_{iso}} A \left[\frac{r}{r_{180}} \right]^{-\alpha} \left[1 + \frac{\alpha(1 + (r/r_{core})^2)}{3\beta(r/r_{core})^2} \right], \quad (6)$$

where $M_{X_{iso}}$ is our original X-ray mass estimate (equation 2). From the data in Figure 7 of Markevitch et al. (1998), we obtain values of 0.4 and 0.5 for α and A , respectively. This new mass estimate is higher than the isothermal estimate at small radii, and lower at larger radii. The difference from the isothermal mass estimates is between -9% and $+29\%$ for individual clusters. For the sample as a whole, the weighted average M_{Dym}/M_X ratio is lowered to 0.96 ± 0.07 . Therefore, if the clusters in our sample at moderate redshift exhibit temperature gradients similar to those seen for rich clusters at low redshift, we can estimate a systematic effect on the average mass ratio of $\lesssim 10\%$ due to large-scale temperature gradients.

5.2.3. Cooling Flows

Our X-ray mass estimates of a cooling flow cluster will be biased relative to a non-cooling flow cluster, as the lower temperature gas in the cooling flow will reduce the value of any emission weighted temperature measurement that is not spatially resolved (as is the case for the low spatial-resolution ASCA observations which we rely on). Multi-phase temperature models have been employed by some authors to attempt to more precisely determine the state of the ICM in cooling flow clusters (e.g. A98; Böhringer et al. 1998). However the additional free parameters associated with a multi-phase fit introduce very high uncertainties in the temperature determinations, and the measured single-phase temperature value cannot be excluded in most cases. Spatially resolved high resolution spectroscopy (as is possible

with AXAF, but not yet available) will be needed to adequately constrain the more complex models.

We can use the $M_{D_{yn}}/M_X$ ratios in subsamples of cooling flow and non-cooling flow clusters to estimate the effects of cooling flows on our results. The dynamical mass is independent of any X-ray temperature bias, and thus we expect to see higher ratios for the cooling flow clusters than for the non-cooling flow clusters due to this effect. We have divided our sample into cooling and non-cooling flow systems. We have classified all those clusters with non-zero inner cutoff radii as listed in Table 3 as cooling flows, with the exception of MS 1006.0+1202, whose suspected cooling flow is very small. We see that our cluster sample is dominated with suspected cooling flows, with only five clusters excepted (including MS 0906.5+1110, which is not included in the averages, and the addition of MS 1006.0+1202 as a non-cooling flow cluster).

Taking weighted averages of the $M_{D_{yn}}/M_X$ mass ratios found in Table 3, we find 1.00 ± 0.08 and 1.15 ± 0.13 for the cooling flow and non-cooling flow systems, respectively. Comparing the two sets of ratios with a K-S test shows that there is a 51% probability that the two sets come from the same parent distribution. Thus we do not detect the expected high ratio for cooling flow clusters, and suggest that this effect is masked by the random uncertainties in the mass estimates.

In order to investigate the possible effects on the subsample $M_{D_{yn}}/M_X$ ratios due to misclassification of cooling flows based on our subjective evaluation of the azimuthally averaged surface brightness profile, we have repeated our calculation with a more strictly delineated cluster sample. We have divided the sample into those clusters with strong detections of extended H α ($L_{H\alpha+[N II]} > 10^{42}$ ergs s $^{-1}$, as measured by D92), those with firm non-detections, and those with missing, weak, or indeterminate detections ($L_{H\alpha+[N II]} < 10^{42}$ ergs s $^{-1}$). The strong detection sample, which we define as definite cooling flows includes Abell 2390, MS 0440.5+0204, MS 0839.8+2938, MS 1224.7+2007, MS 1358.4+6245, and MS 1455.0+2232. The weighted average $M_{D_{yn}}/M_X$ ratio for these clusters is 0.98 ± 0.09 . We see that even with a restricted cooling-flow subsample, the mass ratios are consistent with unity, and we do not infer a large systematic bias due to the emission-weighted temperatures. The non-detection sample, which we define as definite non-cooling flows includes MS 0451.5+0250, MS 0906.5+1110, and MS 1008.1-1224. The weighted average $M_{D_{yn}}/M_X$ ratio for these clusters (excluding MS 0906.5+1110) is 1.17 ± 0.19 , which is also consistent with unity, as well as the larger non-cooling flow subsample identified above.

This contrasts with the results of A98, who find a large correction to the isothermal temperature measurement ($\sim 50\%$), and hence the X-ray masses, when using a multiphase model for the cooling flow clusters in their sample. We note that our cooling flow clusters

may on average be less extreme systems than those investigated by A98, whose cooling flow sample had an average mass deposition rate of $\sim 1700 \text{ M}_{\odot} \text{ yr}^{-1}$. We also note that our comparison of cluster subsamples does not reveal a large discrepancy between cooling and non-cooling flow clusters such as that seen by A98, and we estimate that the systematic effect on our average mass ratio from the temperature measurements of our cooling flow clusters does not exceed $\sim 10\%$, similar to the lowest corrections in A98.

5.2.4. *Non-equilibrium Systems and Cluster Substructure*

A possible complication in comparing cooling flow and non-cooling flow clusters comes from the possibility that all non-cooling flow clusters are significantly out of equilibrium in their cores. A98 suggests that these clusters all have elevated core radii and that X-ray mass estimates in the core will thus be biased significantly low. The effect of core structure should be much smaller on our measurements than for their work, since in general we measure the masses well outside of the core region. However, we searched for evidence of systematic differences in fitted parameters and appearance of the images which might indicate that only the cooling flow clusters are in equilibrium. We do find some differences between cooling flow and non-cooling flow clusters in our sample. We have labeled those clusters exhibiting obvious substructure or asymmetry in their HRI images with an asterisk in Table 3. Unfortunately, this subjective definition is difficult to apply to those clusters with very low signal-to-noise ratio images, such as MS 0302.7+1658. Furthermore, we are in general barely resolving substructure in the cores (being limited by the PSF of the HRI, which is $\sim 15 h^{-1} \text{ kpc}$ at $z = 0.3$), and it is difficult to evaluate the regularity of the core of each cluster. However, some structure is evident upon visual inspection of the HRI images. Of the six clusters with the most obvious substructure or asymmetry, only MS 0015.9+1609 is identified as a cooling flow cluster according to our inner cutoff radius criterion, while none of the six clusters would be defined as a cooling flow cluster according to our stricter $\text{H}\alpha$ luminosity criterion. Thus clusters in our sample that exhibit irregularity in their HRI images are almost always identified as indeterminate or non-cooling flow clusters, consistent with A98’s hypothesis.

But to what extent does this irregularity affect our X-ray mass estimates? If we divide our sample into clusters with very regular appearance and those with the highest degree of irregularity, we may compare the M_{Dyn}/M_X ratios to see if there is a discrepancy. The most regular clusters are Abell 2390, MS 0440.5+0204, MS 0839.8+2938, MS 1224.7+2007, MS 1358.4+6245, MS 1455.0+2232, and MS 1512.4+3647. The irregular clusters are MS 0015.9+1609, MS 0451.5+0250, MS 0451.6-0305, MS 0906.5+1110,

MS 1006.1+1202, and MS 1008.1-1224. Taking weighted averages of the M_{Dyn}/M_X mass ratios, we find 0.98 ± 0.08 and 1.18 ± 0.12 for the regular and irregular subsamples, respectively. Thus the M_{Dyn}/M_X ratios do not appear to be significantly perturbed by substructure or asymmetry.

Nonetheless, non-equilibrium conditions which persist well outside of the cluster core may still affect our mass estimates. While the M_{Dyn}/M_X ratios are in unbiased agreement for our sample, we must ask - could both estimates be wrong due to non-equilibrium? The only way this may systematically affect our average mass ratio estimates by more than the $\sim 15\%$ difference between cooling and non-cooling flow subsamples is if non-equilibrium conditions have simultaneously biased both X-ray and dynamical masses by nearly the same amount. The expectation, however, is that merging and non-spherical systems will affect the dynamical mass estimates much more than the X-ray estimates, in part because of the longer relaxation time for the former, but also because of the different nature of the measurements made. For dynamical mass estimates, a non-spherical and unrelaxed system is prone to having an elevated velocity dispersion measurement due to substructure, as well as the increased difficulty of separating field galaxies from cluster galaxies within a complex velocity distribution. Confusion from this (or simply from not obtaining sufficient numbers of galaxy velocities) can easily increase the measured velocity dispersion by factors of 25-100%, and the corresponding dynamical masses by factors of 1.5–4. On the other hand, numerical simulations suggest that X-ray mass estimates will be less affected by substructure in the cluster gas. Extensive numerical simulations by Evrard & Metzler (1996) have demonstrated that X-ray observations fitted to isothermal β models produce nearly unbiased cluster mass estimates in most cases. The worst biases, of 15–35%, came from measurements at very large radii. Thus we expect that incidences of strong non-uniformity will not easily lead to mass ratios near unity, but instead will bias the M_{Dyn}/M_X ratios high.

The cluster MS 0906.5+1110 may be considered an illustration of the greater effect of major mergers on dynamical masses. This cluster was omitted in our comparison between X-ray and dynamical masses, as well as the analysis of C96, because its velocity dispersion was double-peaked and implausibly large – an excellent candidate for a merging system. Its M_{Dyn}/M_X ratio was found to be 2.76 ± 1.01 , suggesting that the X-ray mass estimate is much less affected by the cluster’s non-equilibrium state.

However, it seems that minor mergers may still produce mass ratios close to unity. The cluster MS 0451.5+0250 also shows signs of a possible core merger, with two very bright BCG-like galaxies and complex X-ray morphology in its center. However, here the galaxy velocity dispersion does not appear to be exceptionally broad, the X-ray contours are smooth in the outer regions, and good fits to a β model were obtained from the PSPC data. Its M_{Dyn}/M_X

ratio is 1.23 ± 0.29 . This cluster may be undergoing a merger which is affecting only the innermost parts of the cluster. In this case it seems more likely that both mass estimates, which are made well outside of the core regions, are unaffected by core substructure, rather than that they are both strongly biased by nearly exactly the same amount.

One more set of independent data can be used to check on whether the mass estimates may be systematically affected by substructure. The total galaxy luminosity should allow a rough cluster mass estimate which is not strongly affected by substructure. C96 report that the dynamical M/L ratios for this sample (omitting MS 0906.5+1110) are consistent with a universal value. This implies that the random measurement uncertainties are larger than any gross errors in the individual cluster dynamical masses due to substructure. We computed the M_X/L ratios for our sample at the same radii at which the M_{Dyn}/M_X ratios have been computed, using data from C96, and also find the distribution to be consistent with random uncertainties. In order to estimate remaining possible systematics in the mass estimates due to substructure, we compared the average M_X/L values for cooling flow and non-cooling flow clusters. If cooling flow clusters are assumed to be equilibrium systems, then the limit of the difference in their M/L ratios sets the maximum effect of non-equilibrium on the non-cooling flow clusters. We found that the ratio of the cooling flow to non-cooling flow M_X/L values is 1.19 ± 0.24 , statistically consistent with no effect, but possibly indicating a small bias. Thus we estimate the maximum systematic in the non cooling flow clusters due to non-equilibrium to be $\sim 25\%$.

5.2.5. *Summary of Possible Systematic Biases*

We have found the effect of the instrumental PSF to be negligible on our data set. Following the assumption of Markevitch et al. (1998) that their observed temperature gradient exists in our cluster sample, we estimate a maximum systematic increase on the weighted average X-ray masses of $\lesssim 10\%$. We have compared cooling and non-cooling flow clusters in our sample and estimate that a failure to account for the lower emission-weighted temperature in cooling flow clusters may decrease the mass ratios for the cooling flow subsample by $\lesssim 10\%$.

Finally, we have discussed the effects of non-equilibrium conditions, particularly in non-cooling flow clusters. If non-equilibrium conditions produce nearly the same bias in both dynamical and X-ray mass estimates, the excellent agreement between their values may not indicate that both estimates are fundamentally correct. We argue that this is not likely to happen in systems with significant merging, as exemplified by the cluster MS 0906.5+1110. Further, we note that the consistent agreement between dynamical and X-ray mass estimates,

and the total cluster galaxy light makes it difficult to argue that any cluster in our sample has an estimated mass which is in error by significantly more than the statistical uncertainties in the measurement. A comparison of cooling flow and non-cooling flow clusters suggests an upper limit on the average mass bias due to non-equilibrium to be $\sim 25\%$.

Combining these possible systematics allows firm limits to be placed on the possibility that these cluster mass estimates are significantly biased. For cooling flow clusters, we estimate a total possible bias in the X-ray measurements of -10% to $+10\%$ (for effects of the cooling flow and large scale temperature gradients, respectively). For non-cooling flow clusters we estimate the possible biases to be no more than -25% (for non-equilibrium) to $+10\%$ (for temperature gradients). We stress once again that these relatively tight limits are probably only made possible by the uniformity of the sample and that a sample with stronger cooling flows, stronger merging systems, or with mass comparisons made closer to the cluster cores might exhibit larger biases.

We note again that the dynamical masses we compare to have been corrected by 16% from the virial mass estimates, following C97. Since this correction is comparable to our possible systematics, we cannot say unequivocally that it is mandated by this comparison, but we note that it is fully consistent with our results.

5.3. Comparison With Gravitational Lensing Measurements

We have also performed a comparison of our masses to the currently available gravitational lensing masses in the literature. Using our fitted parameters, we calculate the projected X-ray mass (based on the derivation in Gioia et al. 1998)

$$M_{X_{proj}}(< r) = 1.74 \times 10^{15} \beta \left[\frac{T}{10 \text{keV}} \right] \left[\frac{r}{\text{Mpc}} \right] \frac{(b/r_{core})^2}{\sqrt{1 + (b/r_{core})^2}} h^{-1} \text{M}_{\odot}, \quad (7)$$

in a cylinder of the same radius, and in the same cosmology, as the given lensing mass estimate. The symbols are the same as in equation (2), and b is the projected radius on the sky. The ratio of gravitational lensing mass to X-ray mass is plotted in Figure 7 as a function of the lensing radius. We find that masses from strong arcs are systematically higher than X-ray masses, by up to a factor of ~ 5 , with most values a factor of ~ 2 higher. Weak lensing estimates are also higher, though the discrepancy is less (factors of ~ 1.5).

Can we understand which estimators are biased, since they do not agree? As can be seen in Figure 7, many of the strong lensing masses are measured at very small radii, in some cases near our inner cutoff for cooling flows. In general, these values show the strongest discrepancies. The nature of our simple isothermal model implies a smooth mass distribution

into the core of the cluster. Large mass clumps inside a few tens of kpc will not be accurately modelled. A98’s analysis of cooling flow clusters yielded core radii typically a factor of 5 smaller than ours (on the order of $25h^{-1}$ kpc), suggesting much more highly concentrated cores than implied by our fits, even after including a correction for the instrumental PSF. This difference in our fitted parameters bears the primary responsibility for our differing results, as the X-ray masses are highly dependent on the value of the core radius when measured at small radii. Clearly the effects of substructure and asymmetry discussed in Section 5.2.4 may affect the X-ray mass estimates more strongly in the cluster cores, possibly accounting for the discrepancy.

However, we note that at somewhat larger radii the enclosed mass is well-constrained by the X-ray profiles, with little dependence on the fitted core radii. We can therefore set strong upper limits on the total cluster mass at radii greater than about $100h^{-1}$ kpc. While a high lensing mass may indicate a strongly peaked mass distribution in the cluster cores, (e.g. Miralde-Escudé & Babul 1995), which the X-ray profile cannot constrain, a lensing mass within a few tens of kpc which is greater than the X-ray derived mass at a much larger radius is difficult to reconcile (e.g. MS 1006.0+1202, see Figure 7).

One significant source of uncertainty in the strong lensing estimates is the lack of redshift information available for many of the lensed arcs. Another important difference in mass estimates may be due to differences in the X-ray and lensing centers of the clusters (see A98 for a discussion). If a large offset (e.g. > 50 kpc) exists between the centers, the two methods will be probing mass distributions through distinctly different lines of sight through the cluster. In this case, one may not expect to be able to perform a meaningful comparison of the cluster mass at small radii. We have listed the sky coordinates of the X-ray centroids for all of our clusters in the Appendix. For the clusters we have in common with Luppino & Gioia (1995), Pierre et al. (1996), and A98, our cluster centers coincide to within a few arcseconds. Fahlman et al. (1994), Smail et al. (1995), Smail et al. (1997), and WF97 do not list the positions they have centered their mass estimates on for the clusters we have in common with them. Asymmetry or substructure in the lens may also lead to overestimates of the lensing mass by factors of ~ 1.6 , as shown by Bartelmann (1995). Finally, strong lenses may preferentially be found in clusters which also have other intervening mass distributions along the line of sight, tending to systematically increase the lensing mass over the cluster mass.

In general we find that the weak lensing estimates are in better agreement with the X-ray and dynamical masses than are the strong lensing mass estimates, although they remain systematically higher. Here the radii of comparison are generally larger than the 2σ radii to which the X-ray mass profiles are measured, and similar to typical radii for dynamical

measurements. Possible reasons for discrepancies may include assumptions in the lensing model about the mass profile in the cluster and uncertainties in the redshift distributions of the lensed sources. Our β -model extrapolation to the quoted weak lensing radii may also be inconsistent with the assumed mass distribution profiles in the different estimates. We suggest that concurrence may be possible with weak lensing estimates, and that constraining the remaining systematics in both methods may resolve the discrepancies. A uniform treatment of the sample is necessary, but unfortunately there is not yet enough information in the literature to explore the comparisons in such a manner. Individual comparisons with both strong and weak lensing mass estimates are presented in the Appendix.

Our results are notably different from those of WF97, who compared lensing, virial, and X-ray mass estimates for a sample of clusters which included seven objects in common with our sample. Their analysis assumed fixed values of β and r_{core} , and temperatures primarily derived from the L_x – T_x relation. They concluded that while dynamical masses appeared to be in agreement with both weak and strong lensing results, X-ray methods underestimated the cluster mass by factors of 2–3. However, their chosen sample is quite heterogeneous, and includes several clusters which may have erroneously high velocity dispersions. This may have biased their dynamical results toward higher values.

Recently, W98 reanalyzed their cluster sample (which now includes nine clusters in common with our sample), and concluded that the X-ray, weak lensing, and dynamical methods are all appropriate and accurate tracers of the gravitational potential at many core radii. Their dynamical/X-ray mass ratios are 1.08 ± 0.7 , in general agreement with our results, but with much larger scatter. We note that the CNOC dynamical masses appear to have much less scatter in the σ – T relation than other clusters in their sample, and suggest again that the CNOC sample provides a much more accurate measure of velocity dispersions than is usually available at these redshifts. We also suggest that the more detailed treatment we have presented of both dynamical and X-ray mass calculations contributes to the much smaller scatter we find in the mass ratios.

At smaller radii, W98 find large discrepancies between strong lensing and X-ray mass estimates, similar to our results, and suggest that this is due to failures in the X-ray analysis to account for the effect of cooling flows on the emission-weighted temperature, or clusters being out of dynamical equilibrium (especially the cores of non-cooling flow clusters), resulting in gross overestimates of the core radius and hence low X-ray mass estimates at small radii. We note that for our sample the effects of the cooling flow temperature bias appear to be at the 10% level, and we suggest that this is not a viable explanation for the lensing/X-ray discrepancy in our sample. Alternatively, we propose that either systematics in the strong lensing mass estimates, or non-equilibrium in the X-ray core structures may be the cause of

the discrepancy.

5.4. Baryon Fractions and Ω_0

Observations of the ICM X-ray emission also allow us to estimate the gas density and the total gas mass in each cluster. Cluster fluxes and luminosities in the ROSAT HRI band (0.1 – 2.4 keV) are listed in Table 4, columns (2) & (3). We model the emission as thermal bremsstrahlung according to a Raymond-Smith plasma (Raymond & Smith 1977) consisting of hot gas at the measured cluster temperature, containing 40% of the Allen (1973) elemental abundance values, and absorbed by cold Galactic hydrogen⁹.

The gas density at a radius r was calculated for a β model (Jones & Forman 1984):

$$\sqrt{n_e n_H(r)} = \left(\frac{\rho_{g0}}{1.244 m_p} \right) [1 + (r/r_{core})^2]^{-3\beta/2} h^{1/2}. \quad (8)$$

Here, ρ_{g0} is the central gas density, which can be described by

$$\rho_{g0} = \left[\frac{S_0 4\pi (1.244 m_p)^2 \Gamma(3\beta) (1+z)^4}{\epsilon_0 \times 10^{-23} \sqrt{\pi} r_c \Gamma(3\beta - 1/2)} \right]^{1/2}, \quad (9)$$

where ϵ_0 is the X-ray volume emissivity coefficient calculated from the most recent Raymond-Smith plasma code¹⁰. We combine this with the gas mass density equation (see Carlberg et al. 1997)

$$\rho_{gas}(r) = 1.244 m_p \sqrt{n_e n_H(r)} h^{1/2} \text{ gm cm}^{-3}, \quad (10)$$

and integrate out to the 2σ cutoff radius to obtain gas masses complementary to the total X-ray cluster masses. These are listed as a fraction of total cluster mass in Table 4, column (4). We have overlaid the radial gas mass profiles on Figure 4 (dotted lines).

For those clusters with suspected cooling flows, we have also estimated the fraction of each cluster’s luminosity attributed to the cooling flow. We measure the total luminosity inside the inner cutoff radius described in §4, and subtract from that the luminosity in the same region we calculate from our fitted β model profile. The net luminosity is then expressed as a fraction of the total cluster luminosity in column (5) of Table 4.

Under the assumption that rich galaxy clusters have collapsed gravitationally from regions of the universe with representative ratios of dark to baryonic matter, we can infer

⁹ N_H values are taken from Dickey & Lockman (1990). The database can be accessed via Starview over the world wide web at <http://skyview.gsfc.nasa.gov/cgi-bin/skvadvanced.pl>

¹⁰Updated 21 Sep., 1993, available at ftp://heasarc.gsfc.nasa.gov/software/plasma_codes/raymond

that the baryon fraction in clusters is equal to that in the field. Neglecting the galaxy mass as small compared to the X-ray emitting gas mass (see David, Jones, & Forman 1995), we equate the baryon fraction with the gas mass fraction. We can then obtain $\Omega_0 = \Omega_b/f_b$ where Ω_b is the mass fraction of the critical density in baryons, and f_b is the measured mass fraction of the universe in baryons. Values of Ω_b can be constrained by Big Bang nucleosynthesis models (c.f. White et al. 1993) as well as light element abundance measurements. Using D/H ratios, Burles & Tytler (1998) finds $\Omega_b h^2 = 0.0193 \pm 0.0014$. A recent review by Olive (1997) suggests the range $0.005 < \Omega_b h^2 < 0.015$ with the most likely value of 0.0065.

From Table 4, the average gas mass fraction for our cluster sample is $0.047 \pm 0.002 h^{-3/2}$, with the uncertainty corresponding to the weighted average uncertainty of the gas fraction among the cluster sample. This is in agreement with typical observed values of $(0.03 - 0.20 h^{-3/2})$, e.g. Sarazin 1988; Böhringer 1994; White & Fabian 1995). Combining the gas mass fraction with the Burles & Tytler (1998) range for Ω_b yields

$$\Omega_0 = 0.41 \pm 0.03 h^{-1/2}. \quad (11)$$

For the wider range suggested by Olive, we find

$$\Omega_0 = 0.14^{+0.18}_{-0.03} h^{-1/2}. \quad (12)$$

We emphasize that the baryon fraction is only measured out to a limited radius within the cluster (the 2σ cutoff), but as can be seen from the mass profiles, the fraction is increasing with radius. With accurate data out to greater radii, we would expect to find somewhat larger baryon fractions, implying that we have actually presented upper limits to the value of Ω_0 . C96 analyzed the CNOC sample and used cluster M/L ratios to obtain $\Omega_0 = 0.19 \pm 0.06$, in general agreement with this work. The addition of galaxy masses would increase the cluster baryon fraction slightly, and lower the value of Ω_0 . The primary statistical uncertainty in total mass is the temperature uncertainty, while for the gas mass it is the uncertainty in β . It should be noted that to achieve $\Omega_0 = 1$ would require a drop in the gas mass relative to the total mass by a factor of $\sim 2 - 3$, clearly not allowed by the data.

6. Conclusions

We have shown that virial cluster masses are in good agreement with the X-ray derived masses in this intermediate redshift sample. The comparison shows no systematic bias, with a weighted average $M_{Dyn}/M_X = 1.04 \pm 0.07$, and no intrinsic scatter in individual M_{Dyn}/M_X ratios is seen beyond the 20 – 30% observed uncertainties. We do note, however, that our observed agreement is dependent on our choice of relatively relaxed systems which have

extensive optical and X-ray observations. We have estimated that systematic errors due to temperature gradients in the ICM, cooling flows, and non-equilibrium states may introduce overall biases of up to +25% and -10% on the M_{Dyn}/M_X ratios. This implies that both detailed dynamical and X-ray mass estimates reflect the true gravitating mass in clusters.

We find that mass estimates from the literature based on gravitational lensing are systematically higher than the other two methods, as has been noted by other authors. However, our X-ray and dynamical data lack resolution on the smallest scales and cannot accurately probe the cluster cores where the strongest discrepancy exists between our methods and strong lensing techniques. We therefore suggest that systematic errors including mass clumps along the line of sight, unknown redshifts in the lensed objects, and difficulties in characterizing the X-ray emission in cluster cores still prevent a detailed comparison of techniques in the small radii regime. The effects of cooling flows and merger events further complicates these studies (A98; W98), although the trend in mass estimates from these effects is not detected in our sample. We suggest that the smaller but non-negligible discrepancy seen with weak lensing is most likely due to uncertainty in the redshift distribution of background galaxies, and inconsistencies in extrapolations along the mass profiles.

The observed baryonic gas fraction in clusters constrains Ω_0 to be less than ~ 0.4 , confirming the severe challenge to closed cosmological models with $\Lambda = 0$ posed by previous efforts.

This research has made use of data obtained through the High Energy Astrophysics Science Archive Research Center Online Service, provided by the NASA/Goddard Space Flight Center. Available at <http://heasarc.gsfc.nasa.gov/cgi-bin/W3Browse/w3browse.pl>. This work was supported by NASA grant NAG5-3161 and NSF grant AST-9617145. We would like to thank the anonymous referee for useful suggestions that helped to improve the paper. ADL wishes to acknowledge Ka Chun Yu for help with figures; and Beth White for her ongoing support.

A. Appendix: Notes on Individual Clusters

A.1. Abell 2390

Abell 2390, at $z=0.23$, is one the best-studied clusters at higher redshifts. It is extremely bright in X-rays, providing one of the highest signal to noise ratio surface brightness profiles in our sample. There are ROSAT HRI, ROSAT PSPC, and ASCA data available. There are multiple arcs and arclets visible that have been used for gravitational lensing studies. It has

been estimated to have a large ($\sim 250h^{-2} \text{ M}_{\odot} \text{ yr}^{-1}$) cooling flow (Pierre et al. 1996; Rizza et al. 1997).

The HRI surface brightness profile is relatively smooth - apparently a good candidate for a simple β model fit. The emission is noticeably elliptical. We see dramatic jumps in emission near the core in this profile. This is probably the signature of the cooling flow, and we have only used data outside of $39h^{-1}\text{kpc}$ for our fit.

Our X-ray centroid lies at R.A.(1950)= $21^h51^m14^s.1$, decl.(1950)= $17^h27^m33^s.1$, which is within one arcsecond of the measurements of Pierre et al. (1996) and A98.

Our fits to β and r_{core} differ with the X-ray analyses of both Rizza et al. (1997) and Pierre et al. (1996) by up to $\sim 30\%$ due to details of the analyses, primarily methods of accounting for the effect of the cooling flow. We note, however, that our mass estimates are in good agreement with both works. We see a large discrepancy between our X-ray analysis and that of A98, who find an r_{core} four times smaller than ours. Combined with their mean temperature of 14.5 keV, compared with the value of 8.9 keV from Mushotzky & Scharf (1997), and a large fitted intrinsic N_H column, this yields a mass profile far in excess of our own. We attribute the difference in r_{core} partly to our subjective method of accounting for the peaked cooling flow on the profile but also note that the A98 r_{core} value is much smaller than values for typical clusters. The details of the A98 spatial analysis are in preparation, and may shed some light on our differences.

Gravitational lensing estimates for the mass based on weak lensing (Squires et al. 1996, with the mass value calculated by WF97) and a strong arc at $z=0.913$ (discovered by Pelló et al. (1991) and with the mass calculation performed by Pierre et al. 1996) are higher than our X-ray mass by a factor of 1.8 and 1.4, at radii of 602 and $92h^{-1} \text{ kpc}$, respectively. A98 also report a mass estimate based on the same strong gravitational arc at a radius of $87h^{-1}\text{kpc}$ which is 2.3 times greater than our X-ray derived estimate.

A.2. MS 0015.9+1609

MS 0015.9+1609, (also CL0016+16), is another well-studied, bright cluster with available HRI, PSPC, ASCA, and lensing data. At $z=0.55$, it is the most distant cluster in our sample. We see evidence in the surface brightness profile for a cooling flow, and we exclude the inner 31 kpc from the fits. Our X-ray centroid lies at R.A.(1950)= $00^h15^m58^s.2$, decl.(1950)= $16^h09^m27^s.1$, which is $\sim 7''$ south of the BCG coordinates given by Gioia & Luppino (1994, G94 hereafter), and $\sim 4''$ south of the HRI coordinates given by Neumann & Böhringer (1997). We note that the HRI image appears to have some asymmetry near the

core, including a knot to the northeast. In addition, this cluster was not observed in H α by D92, making our identification of the peak in the surface brightness profile as a cooling flow somewhat uncertain.

We note that the independent PSPC fitted values for β and r_{core} are significantly higher than the HRI fits. However, upon constraining the PSPC fit with the HRI fitted value of r_{core} , the final fitted β value is consistent with the original HRI β value. The PSPC profile is still very well fit with the final choice of parameters.

Neumann & Böhringer (1997) have completed a similar X-ray analysis using both HRI and PSPC data, and we note that our mass value is well within the errors of their result at a radius of $1.5h^{-1}$ Mpc. Our gas fraction, converted to their cosmology is $0.26 \pm 0.03 h_{50}^{-3/2}$, in agreement with their quoted range of 0.14-0.32 $h_{50}^{-3/2}$.

Smail et al. (1995) analyzed MS 0015.9+1609 using weak lensing, and arrived at a total mass 1.5 times higher than our X-ray mass, at a radius of $334h^{-1}$ kpc. Their more recent analysis (Smail et al. 1997) obtains a mass 1.1 times higher than ours at a radius of $226h^{-1}$ kpc.

A.3. MS 0302.7+1658

The relatively low counts in the HRI exposure of this cluster at $z=0.43$ yield a peaked but not uniform surface brightness profile, from which we exclude the inner $27h^{-1}$ kpc, assuming a cooling flow. Our X-ray centroid lies at R.A.(1950)= $03^h02^m43^s.3$, decl.(1950)= $16^h58^m29^s.4$, which is within $\sim 2''$ of the BCG coordinates given by G94.

This cluster has not been observed by ASCA, and we have used the empirical Bgc- T_x relation (Yee et al. 1999) to estimate the temperature.

A.4. MS 0440.5+0204

This cluster lies at $z=0.20$, and has similarly low HRI counts as MS 0302.7+1658, thus making the estimation of a cooling flow radius somewhat difficult. However the combination of the surface brightness profile and the detection of extended H α emission (D92) lead us to exclude the inner 21 kpc. Our X-ray centroid lies at R.A.(1950)= $04^h40^m33^s.8$, decl.(1950)= $02^h04^m44^s.7$, which is within $\sim 1''$ of the BCG coordinates given by G94. We note that the fitted gas mass fraction for this cluster is the lowest in the sample, achieving a value of $0.026h^{-3/2}$ at $168h^{-1}$ kpc.

Recently, Gioia et al. (1998) analyzed this cluster, and obtained a velocity dispersion of 872 km s^{-1} , 1.4 times higher than that of C96. Upon comparison, we find several common galaxies with identical redshifts, and we can find no a priori reason to discount either value for the velocity dispersion. Thus we have expanded the uncertainty on our velocity dispersion to encompass their value.

Gioia et al. (1998) also performed an analysis of the available ASCA and ROSAT data similar to our own, obtaining significantly smaller values of r_{core} and β , as well as total mass (when we compare at a similar radius). We attribute this to our exclusion of X-ray emission in the core from the fit to the surface brightness profile.

The WF97 review contains a mass estimate within $46h^{-1} \text{ kpc}$ based on a strong arc at $z=0.53$ discovered by Luppino et al. (1993). Their value is 2.5 times our X-ray derived mass at the same radius, in the same cosmology. Gioia et al. (1998) also placed limits from strong lensing on the cluster mass within $52h^{-1} \text{ kpc}$ which were ~ 1.9 times higher than our X-ray estimate.

A.5. MS 0451.5+0250

MS 0451.5+0250 (also Abell 520) at $z=0.20$ exhibits extremely disturbed, clumpy morphology in a relatively short ROSAT HRI exposure, resulting in a surface brightness profile that is not well fit by a β model. We have therefore chosen to use the PSPC data for our fits, but we constrain r_{core} to be $100 \pm 50 \text{ kpc}$ in order to avoid overestimating this parameter due to the large PSF of the instrument. It is also noted in C96 that it contains two dominant galaxies, and two peaks in its galaxy velocity distribution. We suggest this as a strong candidate for a core merger. We also identify it as a non-cooling flow cluster based on the lack of a bright peak in the X-ray surface brightness profile, and a non-detection of $\text{H}\alpha$ by D92. Our X-ray centroid (from the PSPC data) lies at R.A.(1950)= $04^h51^m32^s.4$, decl.(1950)= $02^h50^m18^s.2$, which is within $\sim 30''$ of the optical center given by G94. They note, “There is not a well defined optical center in this cluster but several galaxy condensations are visible.”

Interestingly, the PSPC exposure yields a reasonably smooth surface brightness profile, which is well fit by a β model. We anticipate that future imaging of this cluster with higher resolution instrumentation (e.g. AXAF, XMT) may reveal new insight into merging cluster structure.

A.6. MS 0451.5-0305

The analysis of the PSPC image of this $z=0.54$ cluster by Donahue (1996) revealed one of the first extremely hot, high redshift clusters ever found. There is no evidence of a cooling flow present. Our X-ray centroid lies at R.A.(1950)= $04^h51^m41^s.3$, decl.(1950)= $-03^h05^m54^s.8$, which is within $\sim 15''$ of the optical center given by G94. We attribute this relatively large offset to the non-uniform core of the X-ray image, containing multiple peaks, and exhibiting elongation both N-S and E-W.

The fitted parameter values are markedly different from HRI and PSPC data sets (see Table 2). The combination of the two results in an intermediate value of β which fits both the HRI and the PSPC profiles extremely well. We note that the use of the final parameters from this work results in a total mass at a radius of $1h^{-1}\text{Mpc}$ which is 30% lower than that derived from PSPC data alone by Donahue (1996), though within the somewhat large errors from that work. We have assumed the temperature calculated by Donahue for our analysis.

Strong arc lensing mass estimates from Luppino & Gioia (1995) and WF97 (based on an arc from the Le Fèvre et al. 1994 survey) find values in excess of our X-ray masses by factors of 2.3 and 3.5, at radii of 132 and $106h^{-1}$ kpc, respectively. Redshifts of the lensed arcs are not known.

A.7. MS 0839.8+2938

For the otherwise average cluster MS 0839.8+2938, at $z=0.19$, we estimated a cooling flow cutoff radius of 25 kpc. Our cooling flow identification is supported by the detection of extended $\text{H}\alpha$ emission by D92. Our X-ray centroid lies at R.A.(1950)= $08^h39^m53^s.2$, decl.(1950)= $29^h38^m13^s.7$, which is within $\sim 5''$ of the optical center given by G94.

A.8. MS 0906.5+1110

This cluster at $z=0.17$ exhibits a bimodal galaxy velocity distribution, suggesting a recent merger. The X-ray emission exhibits a significant secondary peak near the center. The surface brightness profile is irregular within the core radius, but has a very smooth tail. We also identify it as a non-cooling flow cluster based on the non-detection of $\text{H}\alpha$ by D92. A detailed substructure analysis may reveal a correlation between the X-ray morphology and galaxy colors and/or velocities. Our X-ray centroid lies at R.A.(1950)= $09^h06^m29^s.8$, decl.(1950)= $11^h10^m43^s.2$, which is within $\sim 5''$ of the optical center given by G94.

This cluster has not been observed by ASCA, and we have used the L_x – T_x relation from Mushotzky & Scharf (1997) to obtain a temperature. Because of the spuriously high velocity dispersion found for the galaxies (C96), we have omitted this cluster from our comparison of dynamical and X-ray mass estimates.

A.9. MS 1006.0+1202

The long pointed exposure of this relatively faint cluster at $z=0.26$ reveals a fair amount of substructure and asymmetry in the HRI image. The resulting surface brightness profile is flattened, yielding the lowest fitted value of β in the sample. There is possible evidence for a very small cooling flow, though it is not definite; there is a weak detection of extended $H\alpha$ from D92. We exclude only the inner $4h^{-1}$ kpc from the fit. This would be another interesting candidate for further study. Our X-ray centroid lies at R.A.(1950)= $10^h06^m07^s.4$, decl.(1950)= $12^h02^m23^s.8$, which is within $\sim 5''$ of the optical center given by G94.

This cluster has not been observed by ASCA, and we have used the Bgc – T_x relation to estimate a temperature.

Three strong arc mass estimates by WF97 (based on the Le Fèvre et al. 1994 survey) have been compared with this work, yielding ratios of 3.5, 3.8 and 4.6, at radii of 42, 74 and $147h^{-1}$ kpc, respectively. The arc redshifts are not known. The extremely high discrepancy here reinforces our opinion that comparison between strong arcs and X-ray mass estimates are not always applicable. Because of the small radius involved, the lensing method is particularly sensitive to the mass distribution model assumed, and can apparently be grossly different from the X-ray derived mass profile. The X-ray mass, in turn, must be extrapolated deep into the core, and cannot account for irregular mass distributions at very small scales which have little power in the overall profile.

A.10. MS 1008.1-1224

An extremely regular cluster in most respects, MS 1008.1-1224, at $z=0.31$ has a characteristically smooth surface brightness profile, no evidence of cooling structure, and mild asymmetry in the HRI image, consisting of faint extended emission to the North. We also identify this cluster as a non-cooling flow based on the non-detection of $H\alpha$ by D92. Our X-ray centroid lies at R.A.(1950)= $10^h08^m05^s.4$, decl.(1950)= $-12^h24^m44^s.6$, which is $\sim 15''$ north of the optical center given by G94, who note “The cluster has a circular distribution of galaxies surrounding a NS-elongated core. There is a secondary clump of galaxies to the

N.” We expect that the northern X-ray emission accounts for the difference in centroids.

The strong arc mass estimate of WF97 (based on a Le Fèvre et al. 1994 arc) is greater than the X-ray mass by a factor of 3.7 at a radius of $138h^{-1}\text{kpc}$. The redshift of the arc is not known.

A.11. MS 1224.7+2007

The HRI image of MS 1224.7+2007, at $z=0.33$ exhibits a strong, radially symmetric core with extremely faint and ragged edges. The surface brightness profile is enigmatic. After extensive investigation, an inner cooling flow cutoff radius of 34 kpc was chosen. The extended $\text{H}\alpha$ emission detected by D92 from this cluster is consistent with a fairly large cooling flow. Our X-ray centroid lies at R.A.(1950)= $12^h24^m42^s.6$, decl.(1950)= $20^h07^m31^s.4$, which is within $\sim 2''$ of the optical center given by G94.

Fahlman et al. (1994) have performed a weak lensing analysis of MS 1224.7+2007, and their mass estimate is 1.7 times greater than ours at a radius of $512h^{-1}\text{kpc}$.

A.12. MS 1358.4+6245

MS 1358.4+6245, at $z=0.33$ exhibits an extremely regular surface brightness profile from its PSPC image, and a fairly disturbed profile from HRI data. The galaxy velocity distribution observed by C96 indicates that there is a small common velocity group south of the optical cluster center. Our X-ray centroid lies at R.A.(1950)= $13^h58^m20^s.6$, decl.(1950)= $62^h45^m33^s.3$, which is within $\sim 5''$ of the optical center given by G94. To account for a cooling flow apparent in both the HRI image and the $\text{H}\alpha$ data from D92, an inner cutoff radius of 36 kpc was adopted.

This cluster also contains a strongly lensed arc with the highest measured redshift known, $z=4.92$ (Franx et al. 1997). A98 have performed a strong lensing analysis of MS 1358.4+6245, obtaining a mass 1.7 times greater than ours at a radius of $65h^{-1}\text{kpc}$. They also perform an X-ray deprojection analysis, obtaining a mass 3.8 times higher than ours at $65h^{-1}\text{kpc}$. The mean temperature in our analyses differs by only $\sim 15\%$. However, the Allen fitted value for r_{core} is 5.2 times smaller than our fitted value. The HRI surface brightness profile of MS 1358.4+6245 indicates a very peaked core, with significant irregularity directly around it, followed by a reasonably smooth tail. Because the strong lensing probes only the very core of the cluster, we may be seeing very pronounced effects due to subclumping, which our cooling flow cutoff method does not account for. We emphasize, however, that the well

measured dynamical mass is in excellent agreement with our X-ray derived mass at a radius of $240h^{-1}\text{kpc}$. In this case, our X-ray analysis may only provide strong constraints on the mass distribution at larger radii.

A.13. MS 1455.0+2232

MS 1455.0+2232 at $z=0.26$, displays the highest signal to noise ratio HRI surface brightness profile in this sample after Abell 2390. It is highly radially symmetric, and strongly peaked. This cluster has the highest $\text{H}\alpha$ luminosity and the largest $\text{H}\alpha$ extent among the D92 sample. Allen et al. (1996) estimate it to have one of the largest cooling flows known, $\sim 1500 \text{ M}_{\odot}\text{yr}^{-1}$. Our X-ray centroid lies at R.A.(1950)= $14^{\text{h}}55^{\text{m}}00^{\text{s}}.4$, decl.(1950)= $22^{\text{h}}32^{\text{m}}36^{\text{s}}.0$, which is within $\sim 5''$ of the optical center given by G94. The HRI surface brightness profile is extremely well constrained by the slope of the profile, and the values of the fitted parameters are insensitive to choice of inner cutoff radius out to a value of 103 kpc. Therefore, based on the surface brightness profile, we have chosen a cutoff of only 20 kpc, which provides a good statistical fit to the HRI data.

Our mass estimate is in close agreement with the X-ray derived mass estimate of Allen et al. (1996), differing by only 5%. The gravitational lensing mass estimates, based on a strong arc of unknown redshift at $52h^{-1}\text{kpc}$ (WF97, from an arc in the Le Fèvre et al. 1994 survey) and weak lensing observed by Smail et al. (1995) at $237h^{-1}\text{kpc}$, are larger by factors of 1.8 and 1.3, respectively.

A.14. MS 1512.4+3647

The HRI image of MS 1512.4+3647, at $z=0.37$ is somewhat elliptical, uniform, and mildly peaked. There is evidence for a small cooling flow, and the parameter fits are only mildly sensitive to inner cutoff radius. There is a weak detection of extended $\text{H}\alpha$ emission by D92. We have excluded the inner $11h^{-1}\text{kpc}$ from the fits. Our X-ray centroid lies at R.A.(1950)= $15^{\text{h}}12^{\text{m}}26^{\text{s}}.0$, decl.(1950)= $36^{\text{h}}47^{\text{m}}24^{\text{s}}.7$, which is within $\sim 5''$ of the optical center given by G94.

Hamana et al. (1997) perform a similar X-ray analysis, yielding a total mass within $315h^{-1}\text{kpc}$ which is 3% less than our own. We note that their gas mass fraction of 20% is a factor of ~ 3 higher than our estimate. The difference between our analyses may hinge on the neutral hydrogen absorption of the cluster, which we assume to be the value from Dickey & Lockman (1990), and which they leave as a free parameter in their fit.

Hamana et al. (1997) also make use of a PSPC image to supplement their analysis. We have chosen not to include these data, due to the brevity of the PSPC exposure, and the fact that the cluster is not centered in the field of view, making accurate flat fielding even more difficult. Note that the inclusion of PSPC data does not significantly change their parameter fits, yielding a total mass in close agreement with our result.

REFERENCES

- Allen, C. W. 1973, *Astrophysical Quantities*, 3rd ed. (London: Althone Press)
- Allen, S. W. 1998, MNRAS, 296, 392 (A98)
- Allen, S. W., Fabian, A. C., Edge, A. C., Bautz, M. W., Furuzawa, A., & Tawara, Y. 1996, MNRAS, 283, 263
- Bahcall, J. & Sarazin, C. 1977, ApJ, 213, 137
- Balogh, M. L., Morris, S., Yee, H. K. C., Carlberg, R. G., Ellingson, E. 1997, ApJ, 488, L75
- Bartelmann, M. 1995, A&A, 299, 11
- Böhringer, H. 1994, “*Cosmological Aspects of X-ray Clusters of Galaxies*” ed. W.C. Seitter, (London: Kluwer Academic Publishers)
- Böhringer, H., Tanaka, Y., Mushotzky, R. F., Ikebe, Y., & Hattori, M. 1998, A&A, 334, 789
- Burles, S. & Tytler, D. 1998, ApJ, 499, 699
- Carlberg, R. G., Yee, H. K. C., & Ellingson, E. 1994, ApJ, 437, 63
- Carlberg, R. G., Yee, H. K. C., & Ellingson, E. 1997, ApJ, 478, 462 (C97)
- Carlberg, R. G., Yee, H. K. C., Ellingson, E., Abraham, R., Gravel, P., Morris, S., & Pritchett, C.J. 1996, ApJ, 462, 32 (C96)
- Carlberg, R. G., et al. 1997, ApJ, 485, L13
- Cavaliere, A. & Fusco-Femiano, R. 1976, A&A, 49, 137
- David, L. P., Jones, C., & Forman, W. 1995, ApJ, 445, 578
- David, L. P., Jones, C., & Forman, W. 1996, ApJ, 473, 692
- Dickey, J. & Lockman, F. 1990, ARA&A, 28, 215

- Donahue, M. 1996, *ApJ*, 468, 79
- Donahue, M., Stocke, J. T., & Gioia, I. M. 1992, *ApJ*, 385, 49 (D92)
- Evrard, A. E. & Metzler, C. A. 1996, *ApJ*, 469, 494
- Fahlman, G., Kaiser, N., Squires, G., & Woods, D. 1994, *ApJ*, 462, 56
- Franx, M., Illingworth, G. D., Kelson, D. D., Van Dokkum, P. G., & Tran, K. V. 1997, *ApJ*, 486, L75
- Gioia, I. M., Henry, J. P., Maccacaro, T., Morris, S. L., Stocke, J. T., & Wolter, A. 1990, *ApJ*, 356, L35
- Gioia, I. M., Shaya, E. J., Le Fèvre, O., Falco, E. E., Luppino, G. A., & Hammer, F. 1998, *ApJ*, 497, 573
- Gioia, I. M. & Luppino, G. A., 1994, *ApJS*, 94, 583 (G94)
- Hamana, T., Hattori, M., Ebeling, H., Henry, J.P., Futamase, T., & Shioya, Y. 1997, *ApJ*, 484, 574
- Heckman, T. M., Baum, S. A., Van Breugel, W. J. M., & McCarthy, P. 1989, *ApJ*, 338, 48
- Henry, J. P., Gioia, I. M., Maccacaro, T., Morris, S. L., Stocke, J. T., & Wolter, A. 1992, *ApJ*, 386, 408
- Henry, J. P. 1997, *ApJ*, 489, L1
- Jones, C., & Forman, W. 1984, *ApJ*, 276, 38
- Le Fèvre, O., Hammer, F., Angonin, M. C., Gioia, I. M., & Luppino, G. A. 1994, *ApJ*, 422, L5
- Luppino, G. A., Gioia, I. M., Annis, J., Le Fèvre, O., & Hammer, F. 1993, *ApJ*, 416, 444
- Luppino, G. A. & Gioia, I. M. 1995, *ApJ*, 445, L77
- Markevitch, M., Forman, W. R., Sarazin, C. L., & Vikhlinin, A. 1998, *ApJ*, 503, 77
- Miralde-Escudé, J., & Babul, A. 1995, *ApJ*, 449, 18
- Mushotzky, R. F., & Scharf, C. A. 1997, *ApJ*, 482, L13
- Navarro, J. F., Frenk, C. S., & White, S. D. M. 1996, *ApJ*, 462, 563

- Neumann, D. M., & Böhringer, H. 1997, MNRAS, 289, 123
- Olive, K. A. 1997, astro-ph 9707212
- Oukbir, J. & Blanchard, A. 1997, A&A, 317, 1
- Raymond, J. C., & Smith, B. W. 1977, ApJS, 35, 419
- Rizza, E., Burns, J. O., Ledlow, M. M., Owen, F. N., & Voges, W. 1997, MNRAS, preprint
- Pelló, R., Le Borgne, J. F., Soucail, G., Mellier, Y., & Sanahuja, B., 1991, ApJ, 366, 405
- Pierre, M., Le Borgne, J. F., Soucail, G., & Kneib, J. P. 1996, A&A, 311, 413
- Sadat, R., Blanchard, A., & Oukbir, J. A&A, 329, 21
- Sarazin, C. L., 1988, “*X-ray emissions from clusters of galaxies*”, (Cambridge: Cambridge University Press)
- Smail, I., Ellis, R. S., Dressler, A., Couch, W. J., Oemler, A., Sharples, R. M., & Butcher, H. 1997, ApJ, 479, 70
- Smail, I., Ellis, R. S., Fitchett, M. J., & Edge, A. C. 1995, MNRAS, 273, 277
- Snowden, S., McCammon, D., Burrows, D. N., & Mendenhall, J. A. 1994, ApJ, 424, 714
- Squires, G., Kaiser, N., Fahlman, G., Babul, A., & Woods, D. 1996, ApJ, 469, 73
- White, S. D. M., & Fabian, A. C. 1995, MNRAS, 273, 72
- White, S. D. M., Navarro, J. F., Evrard, A. E., & Frenk, C. S. 1993, Nature, 366, 429
- Wu, X.P., Chiueh, T., Fang, L. Z., & Xue, Y. J. 1998, MNRAS accepted, astro-ph 9808179 (W98)
- Wu, X. P., & Fang, L. Z. 1997, ApJ, 483, 62 (WF97)
- Yee, H. K. C., Ellingson, E., & Carlberg, R. G. 1996, ApJS, 102, 269
- Yee, H. K. C., & Green, R. F. 1987, AJ, 319, 28
- Yee, H. K. C., & Lopez-Cruz, O. 1998, AJ, submitted
- Yee, H. K. C. et al. 1999, in preparation

Fig. 1.— HRI Images of the CNOC clusters with X-ray contours overlaid. Images have been blocked by a factor of 8, and smoothed with a 1 pixel FWHM gaussian. The dashed circles represent the 2σ radius for each cluster, defined in §5. These circles are omitted for MS 1231.3+1542 and MS 1621.5+2640 as the data were insufficient for analysis of the surface brightness profiles. For Abell 2390, the circle extends beyond the boundary of the figure. Contours are in units of counts $\text{s}^{-1} \text{ arcmin}^{-2}$. For Abell 2390 the contours start at 0.05, and increase in linear steps of 0.05. MS 0015.9+1609: lowest contour at 0.025 with steps of 0.01. MS 0302.7+1658: lowest contour at 0.024 with steps of 0.003 MS 0440.5+0204: lowest contour at 0.03 with steps of 0.015. MS 0451.5+0250: lowest contour at 0.04 with steps of 0.01. MS 0451.6-0305: lowest contour at 0.03 with steps of 0.008. MS 0839.8+2938: lowest contour at 0.04 with steps of 0.03. MS 0906.5+1110: lowest contour at 0.035 with steps of 0.01. MS 1006.0+1202: lowest contour at 0.035 with steps of 0.005. MS 1008.1-1224: lowest contour at 0.03 with steps of 0.008. MS 1224.7+2007: lowest contour at 0.035 with steps of 0.01. MS 1231.3+1542: lowest contour at 0.033 with steps of 0.003. MS 1358.4+6245: lowest contour at 0.04 with steps of 0.02. MS 1455.0+2232: lowest contour at 0.05 with steps of 0.1. MS 1512.4+3647: lowest contour at 0.03 with steps of 0.02 MS 1621.5+2640: lowest contour at 0.027 with steps of 0.003.

Fig. 2.— X-ray surface brightness profiles with β -model fits overlaid. The solid curve corresponds to the fit when all data points are included. The dotted curve (where applicable) is the fit when inner data points have been excluded from the fit based on our subjective criterion for a cooling flow (see section 3). The solid vertical line indicates the radius at which the fitted profile drops to 2σ above the measured background noise. The dash-dotted vertical line indicates (where applicable) the inner cutoff radius for the suspected cooling flow. Horizontal lines correspond to the measured mean background value.

Fig. 3.— $\text{H}\alpha$ /X-ray Luminosity Ratio vs. Cooling Flow Cutoff radius. The y-axis is the ratio of $\text{H}\alpha$ luminosity (from Donahue et al. 1992) to X-ray Luminosity in the *Einstein* IPC 0.3–3.5 keV band. The x-axis indicates the radius, in kpc, of the subjectively defined inner cooling flow cutoff.

Fig. 4.— Radial mass profiles for the cluster sample. The solid line represents the total mass distribution derived from the X-ray data, the dashed line the mass distribution derived from dynamical data, and the dotted line represents the X-ray derived gas mass distribution. Vertical lines have the same meaning as in Figure 2.

Fig. 5.— M_{Dyn}/M_X ratio vs. X-ray derived mass within the HRI 2σ radius. Errors on each ratio include the 1σ errors from the β model fit and the X-ray temperatures (see Table 2) as well as the uncertainties from the dynamical mass estimates.

Fig. 6.— M_{Dyn}/M_X ratio vs. the HRI 2σ radius at which M_X is measured for each cluster. Errors are the same as in figure 5.

Fig. 7.— Gravitational lens mass/X-ray derived mass ratio vs. radius. The y-axis is the ratio of the published gravitational lensing mass estimates to our X-ray derived mass at the same radius, and in the same cosmology. The x-axis is the radius of the lensing mass estimate in our cosmology ($h = 100$, $q_0 = 0.1$). Note that some clusters have gravitational lens mass estimates at multiple radii and hence are represented by more than one data point. Error bars on the mass ratios include both the lensing mass error and the X-ray derived mass error, and are only plotted where a gravitational lens mass error was available. For reference, error bars for the X-ray masses are indicated in Figure 5. Filled triangles represent strong lensing observations where the redshift of the lensed arc was known, unfilled triangles represent strong lensing of an arc of unknown redshift, and filled squares represent weak lensing analyses. To the right of each data point is the cluster name. To the left of each data point is the reference for the lensing data: (1) Wu & Fang 1997; (2) Pierre et al. 1996; (3) Smail et al. 1995; (4) Smail et al. 1997; (5) Luppino & Gioia 1995; (6) Fahlman et al. 1994; (7) A98; (8) Gioia et al. 1998.

Table 1. Cluster Sample

Cluster	z	L_x ^a	HRI Exposure ^b	PSPC Exposure ^b
Abell 2390	0.2279	5.5	32904	9287
MS 0015.9+1609	0.5466	14.6	73333	41405
MS 0302.7+1658	0.4246	5.0	32706	...
MS 0440.5+0204	0.1965	4.0	26333	...
MS 0451.5+0250	0.2010	7.0	12084	4743
MS 0451.6-0305	0.5392	20.0	45371	15296
MS 0839.8+2938	0.1928	5.4	18797	...
MS 0906.5+1110	0.1709	5.8	78218	...
MS 1006.0+1202	0.2605	4.8	79903	...
MS 1008.1-1224	0.3062	4.5	66780	...
MS 1224.7+2007	0.3255	4.6	52256	...
MS 1231.3+1542	0.2350	2.9	62967	1246
MS 1358.4+6245	0.3290	10.6	28858	21709
MS 1455.0+2232	0.2570	16.0	14703	...
MS 1512.4+3647	0.3726	4.8	34035	5230
MS 1621.5+2640	0.4274	4.5	43256	...

^a 10^{44} erg s⁻¹ in the *Einstein* IPC band (0.3 – 3.5 keV).

^bCorrected exposure time in seconds (see text for corrections applied).

Table 2. Fitted β Model Parameters

Cluster	HRI β^a	HRI r_{core}^a	PSPC β^b	PSPC r_{core}^b	Final β^c	Final r_{core}^c	Temperature ^d	Ref.
Abell 2390	0.61 \pm 0.02	100 \pm 7	0.69 \pm 0.03	138 \pm 13	0.62 $^{+0.01}_{-0.01}$	103 $^{+4}_{-10}$	8.9 $^{+0.5}_{-0.4}$	1
MS 0015.9+1609	0.87 \pm 0.08	214 \pm 24	0.90 \pm 0.04	255 \pm 16	0.81 $^{+0.02}_{-0.08}$	196 $^{+5}_{-23}$	8.0 $^{+0.5}_{-0.5}$	1
MS 0302.7+1658	0.68 \pm 0.15	35 \pm 19	0.68 \pm 0.15	35 \pm 19	3.8 $^{+1.6}_{-1.6}$	5
MS 0440.5+0204	0.68 \pm 0.10	54 \pm 16	0.68 $^{+0.10}_{-0.10}$	54 $^{+16}_{-16}$	5.3 $^{+0.6}_{-0.4}$	1
MS 0451.5+0250	0.80 \pm 11.1	235 \pm 926	0.49 $^{+0.08}_{-0.08}$	100 $^{+50}_{-50}$	0.49 $^{+0.08}_{-0.08}$	100 $^{+50}_{-50}$	8.6 $^{+0.5}_{-0.5}$	1
MS 0451.6-0305	0.80 \pm 0.07	165 \pm 18	0.92 \pm 0.11	189 \pm 30	0.84 $^{+0.06}_{-0.06}$	175 $^{+14}_{-15}$	10.4 $^{+0.8}_{-0.7}$	2
MS 0839.8+2938	0.81 \pm 0.16	69 \pm 20	0.81 \pm 0.16	69 \pm 20	4.2 $^{+0.2}_{-0.2}$	1
MS 0906.5+1110	0.93 \pm 0.07	147 \pm 11	0.93 \pm 0.07	147 \pm 11	8.0 $^{+2.0}_{-1.0}$	3
MS 1006.0+1202	0.67 \pm 0.05	165 \pm 18	0.67 \pm 0.05	165 \pm 18	7.2 $^{+1.6}_{-1.6}$	5
MS 1008.1-1224	0.68 \pm 0.05	124 \pm 14	0.68 \pm 0.05	124 \pm 14	7.3 $^{+1.2}_{-0.8}$	1
MS 1224.7+2007	0.58 \pm 0.10	63 \pm 29	0.58 \pm 0.10	63 \pm 29	4.3 $^{+0.7}_{-0.6}$	4
MS 1358.4+6245	0.84 \pm 0.15	137 \pm 31	0.75 \pm 0.03	107 \pm 8	0.83 $^{+0.11}_{-0.10}$	133 $^{+21}_{-20}$	6.5 $^{+0.3}_{-0.3}$	1
MS 1455.0+2232	0.66 \pm 0.03	40 \pm 4	0.66 \pm 0.03	40 \pm 4	5.5 $^{+0.2}_{-0.1}$	1
MS 1512.4+3647	0.55 \pm 0.04	29 \pm 7	0.55 \pm 0.04	29 \pm 7	3.6 $^{+0.7}_{-0.4}$	1
Average Values	0.72 $^{+0.11}_{-0.08}$	103 \pm 57	0.75 \pm 0.16	158 \pm 58	0.72 \pm 0.08	103 \pm 58	6.5 \pm 2.1	

^aIndependent HRI data, r_{core} in h^{-1} kpc

^bIndependent PSPC data, r_{core} in h^{-1} kpc

^cWhere PSPC data are available, these parameters are fit with combined data, using the HRI r_{core} value to retrieve fitted β value from the PSPC profile. For MS 0451.5+0250 the independent PSPC data is used with a fixed core radius of 100 \pm 50 kpc - see Appendix.

^dMean ASCA cluster Temperature in keV, except as noted.

^eSource for Temperature value.

Note. — Uncertainties in all columns are 1 σ . MS 0451.5+0250 has been excluded from the average calculation of HRI parameters.

References. — (1) Mushotzky & Scharf 1997; (2) Donahue 1996; (3) L_x - T_x relation, e.g. Mushotzky & Scharf 1999; (4) Henry 1997, (5) Bgc- T_x relation, Yee et al. 1999

Table 3. Cluster Masses

Cluster ^a	Inner Cutoff Radius h^{-1} kpc	HRI 2σ Radius h^{-1} kpc	X-ray Mass $10^{14}h^{-1}M_{\odot}$ (HRI 2σ)	Dynamical/X-ray Mass Ratio (HRI 2σ)	PSPC 2σ Radius h^{-1} kpc	X-ray Mass $10^{14}h^{-1}M_{\odot}$ (PSPC 2σ)
Abell 2390	39	526	$3.17^{+0.18}_{-0.15}$	$1.09^{+0.13}_{-0.13}$	1283	8.40 ± 0.49
MS 0015.9+1609*	31	482	$3.02^{+0.20}_{-0.36}$	$1.30^{+0.26}_{-0.29}$	1317	8.67 ± 0.60
MS 0302.7+1658	27	141	$0.39^{+0.19}_{-0.19}$	$0.69^{+0.40}_{-0.40}$
MS 0440.5+0204	21	168	$0.62^{+0.12}_{-0.10}$	$0.47^{+0.29}_{-0.12}$
MS 0451.5+0250*	...	400	$1.81^{+0.32}_{-0.31}$	$1.23^{+0.29}_{-0.29}$	1170	7.50 ± 0.70
MS 0451.6-0305*	...	402	$3.34^{+0.35}_{-0.31}$	$1.22^{+0.24}_{-0.23}$	761	6.62 ± 0.58
MS 0839.8+2938	25	170	$0.56^{+0.11}_{-0.11}$	$0.68^{+0.26}_{-0.26}$
MS 0906.5+1110*	...	300	$2.04^{+0.53}_{-0.30}$
MS 1006.0+1202*	4	459	$2.23^{+0.55}_{-0.55}$	$0.98^{+0.30}_{-0.30}$
MS 1008.1-1224*	...	361	$1.82^{+0.34}_{-0.23}$	$1.13^{+0.28}_{-0.23}$
MS 1224.7+2007	30	199	$0.51^{+0.12}_{-0.12}$	$1.20^{+0.51}_{-0.51}$
MS 1358.4+6245	36	286	$1.46^{+0.21}_{-0.19}$	$0.93^{+0.18}_{-0.16}$	764	4.09 ± 0.38
MS 1455.0+2232	20	260	$1.03^{+0.06}_{-0.05}$	$1.34^{+0.26}_{-0.26}$
MS 1512.4+3647	11	237	$0.52^{+0.11}_{-0.07}$	$1.17^{+0.59}_{-0.55}$
Weighted Average		1.04 ± 0.07

^aClusters exhibiting obvious substructure or asymmetry in their HRI images are denoted with an asterisk.

Note. — Uncertainties for all masses are 1σ . Uncertainty in the average value is the uncertainty in the mean. MS 0906.5+1110 has been excluded from the dynamical/X-ray mass ratio average because the optical data does not constrain the virial mass.

Table 4. Flux, Luminosity, Gas Fractions, Cooling Flow Luminosity Fractions

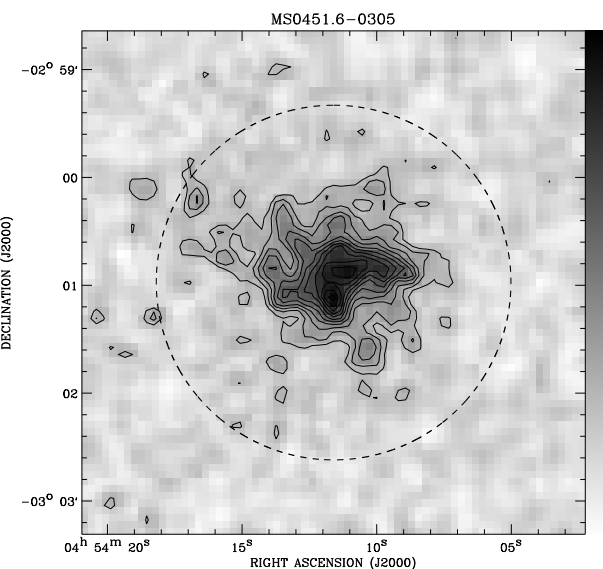
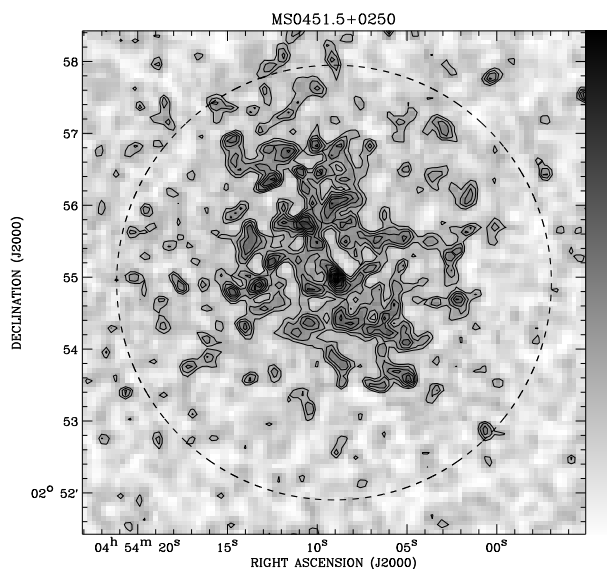
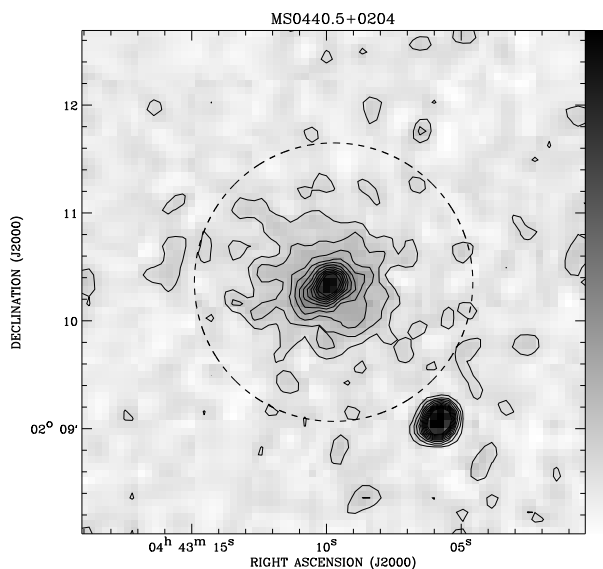
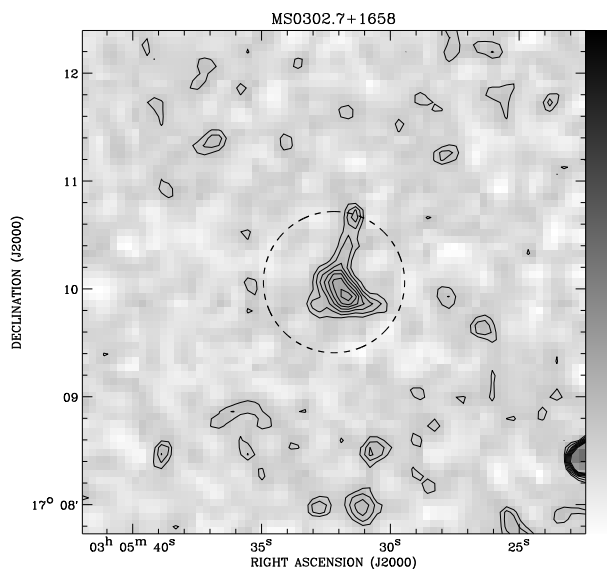
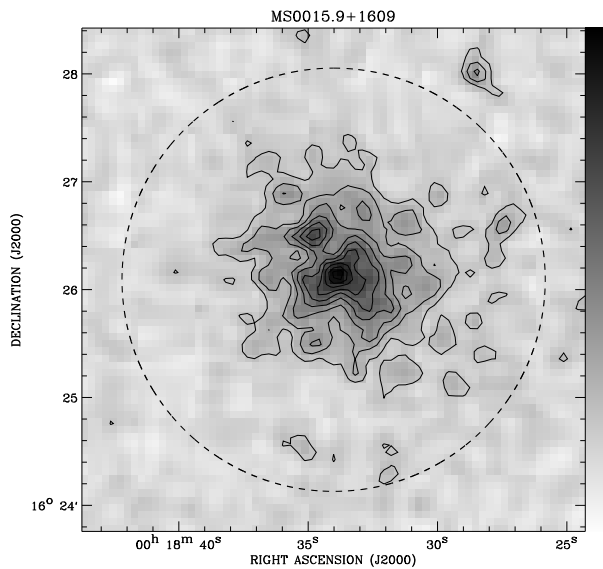
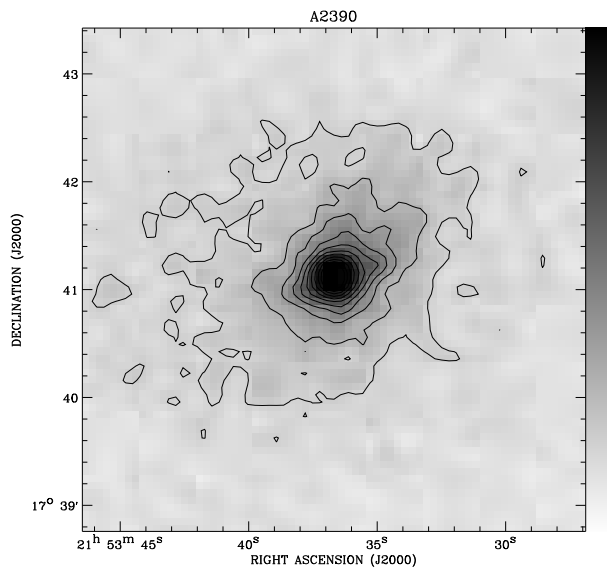
Cluster	HRI $f_x \times 10^{-12}$ erg s ⁻¹ cm ⁻² 0.1 – 2.4 keV ^a	HRI $L_x \times 10^{44}$ erg s ⁻¹ 0.1 – 2.4 keV ^b	Gas Mass Fraction HRI 2- σ Radius $h^{-3/2}$	Cooling Flow Luminosity Fraction ^c
Abell 2390	13.72	11.87	0.089±0.008	0.075±0.003
MS 0015.9+1609	2.72	14.00	0.092±0.010	0.018±0.002
MS 0302.7+1658	0.39	1.63	0.039±0.088	0.000±0.000
MS 0440.5+0204	1.61	1.17	0.026±0.024	0.088±0.011
MS 0451.5+0250	8.77	6.05	0.074±0.012	...
MS 0451.6-0305	2.39	12.01	0.067±0.008	...
MS 0839.8+2938	2.81	17.04	0.033±0.020	0.141±0.013
MS 0906.5+1110	6.76	3.09	0.028±0.003	...
MS 1006.0+1202	6.00	6.35	0.064±0.009	0.001±0.001
MS 1008.1-1224	3.22	5.37	0.054±0.009	...
MS 1224.7+2007	9.19	1.58	0.037±0.245	0.187±0.023
MS 1358.4+6245	2.42	3.86	0.047±0.010	0.138±0.012
MS 1455.0+2232	6.70	6.91	0.076±0.016	0.054±0.004
MS 1512.4+3647	1.15	2.47	0.069±0.032	0.019±0.004
Average Values	0.047±0.002	...

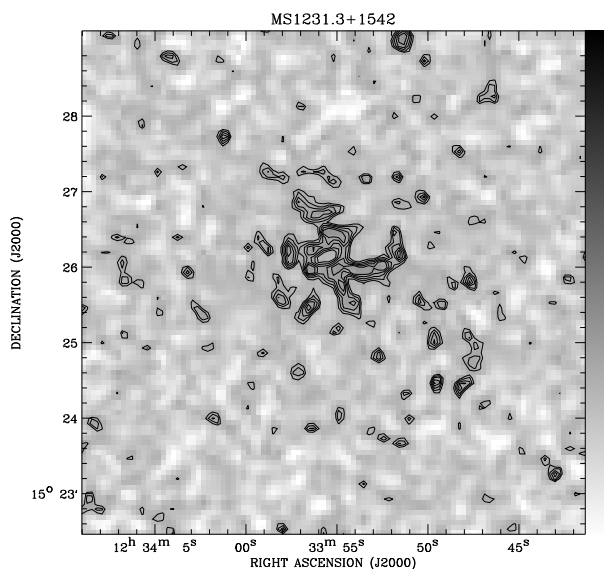
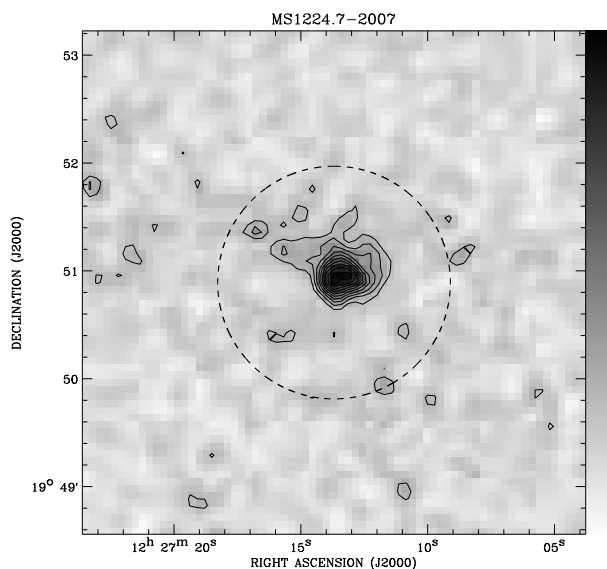
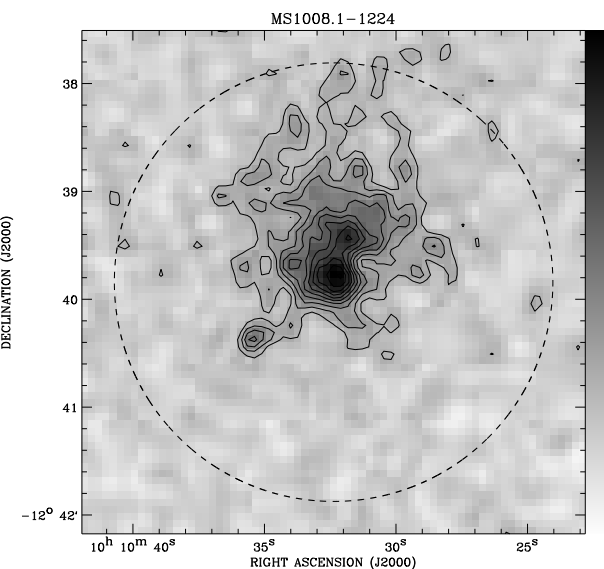
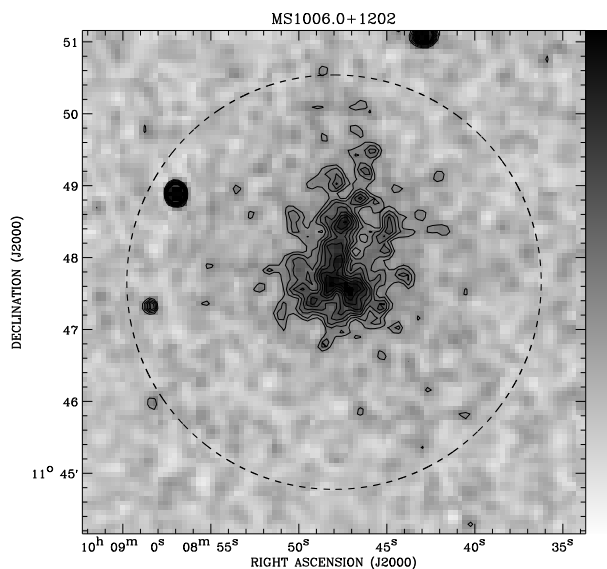
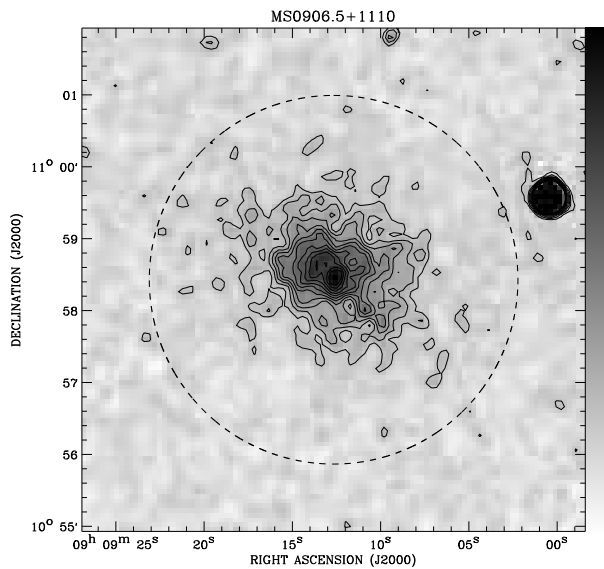
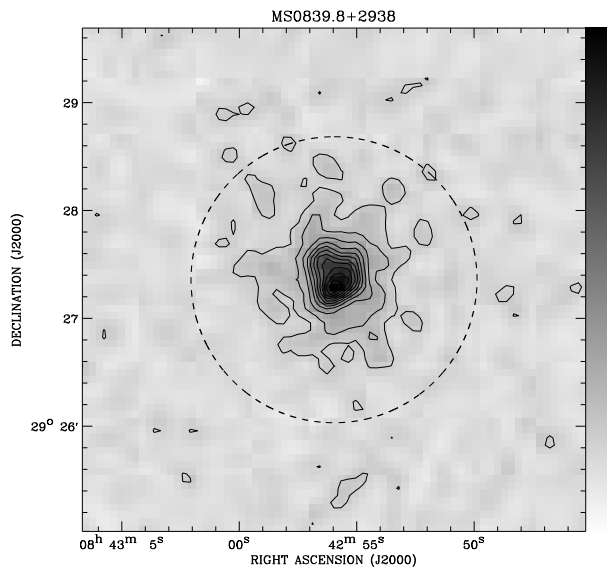
^aThe flux calculated includes absorption by Galactic hydrogen. N_H values are taken from Dickey & Lockman (1990).

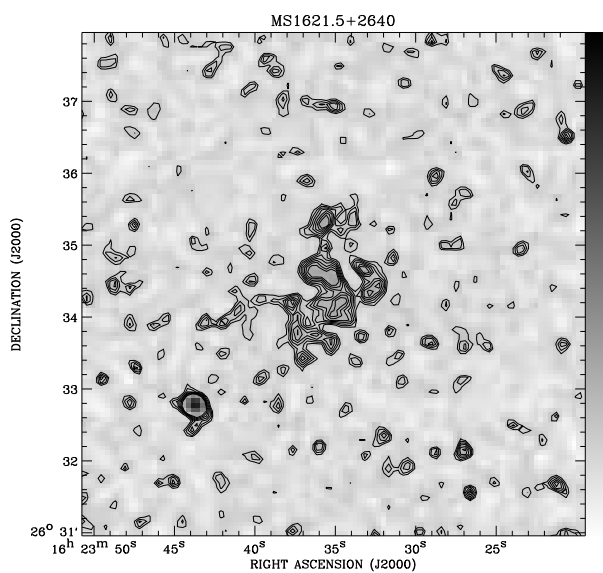
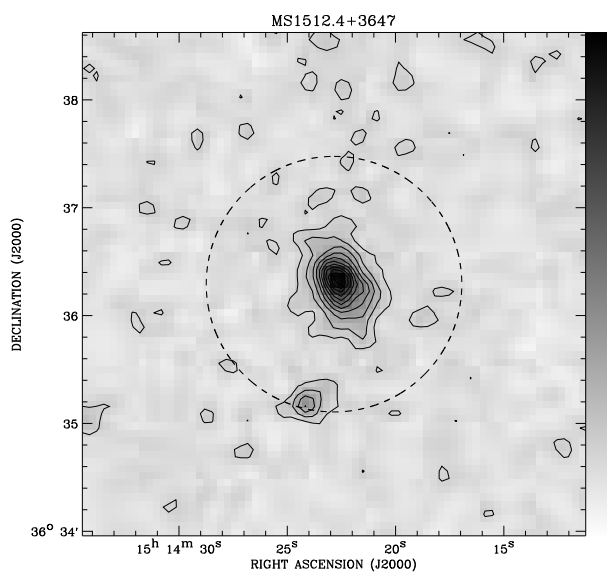
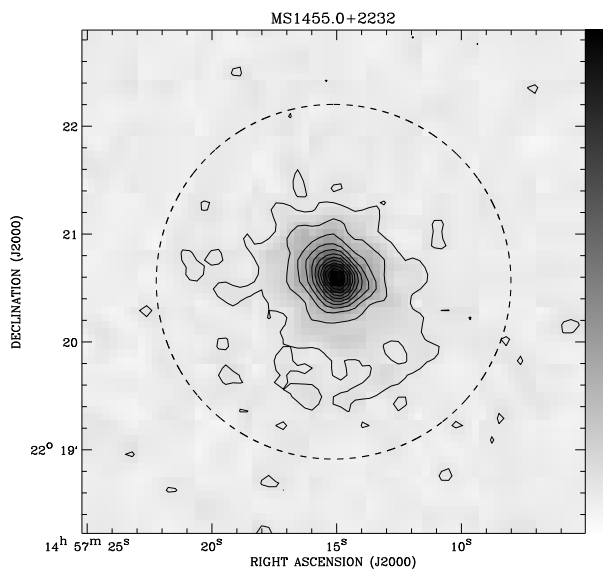
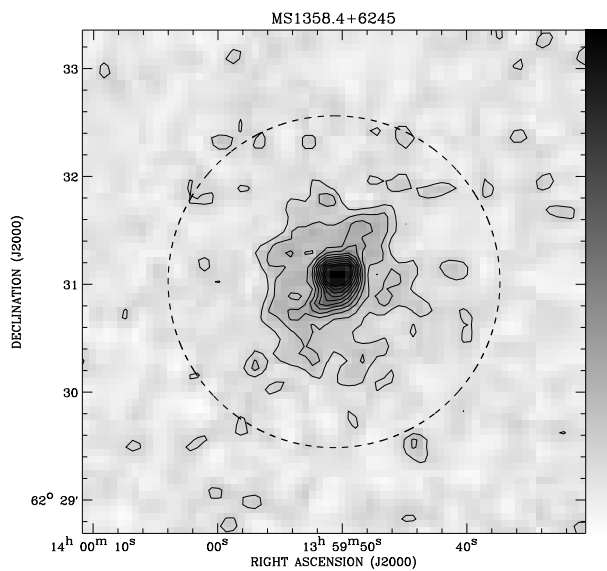
^bThe luminosity is calculated in the rest frame of the cluster.

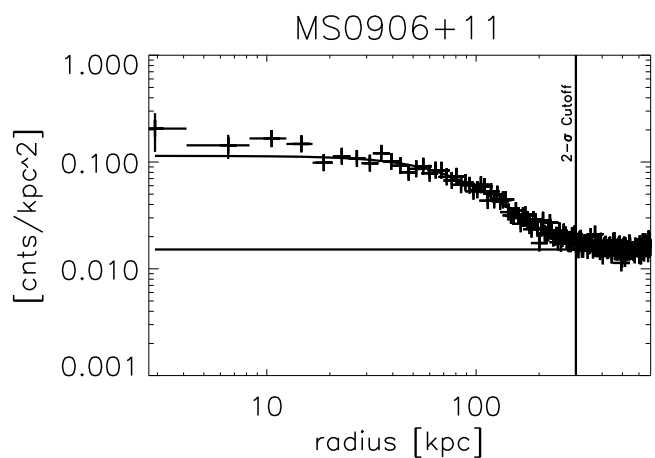
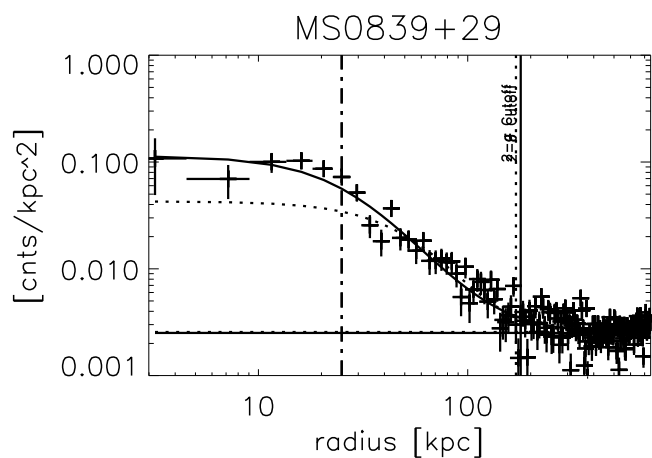
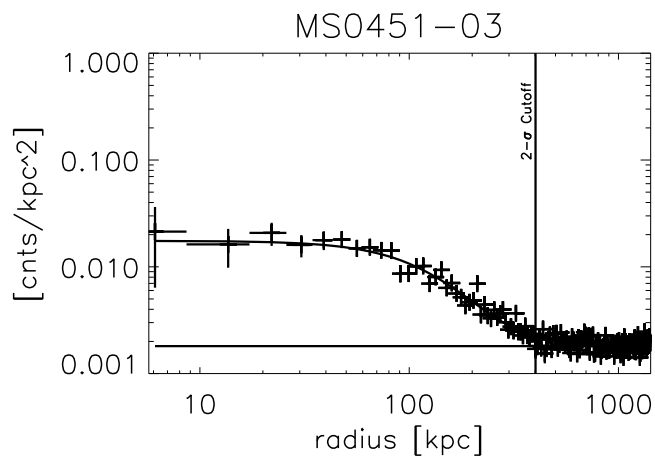
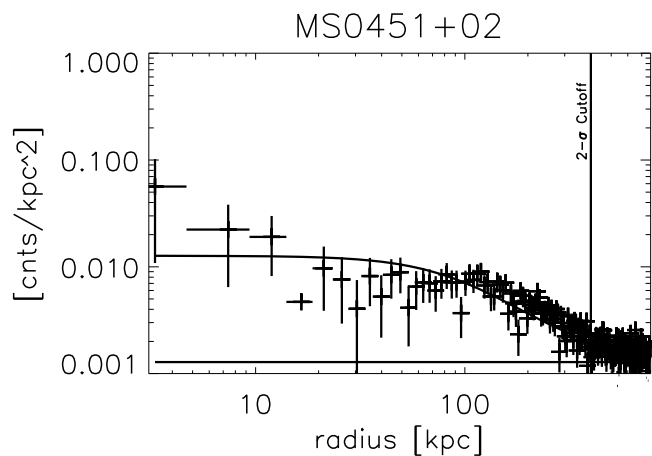
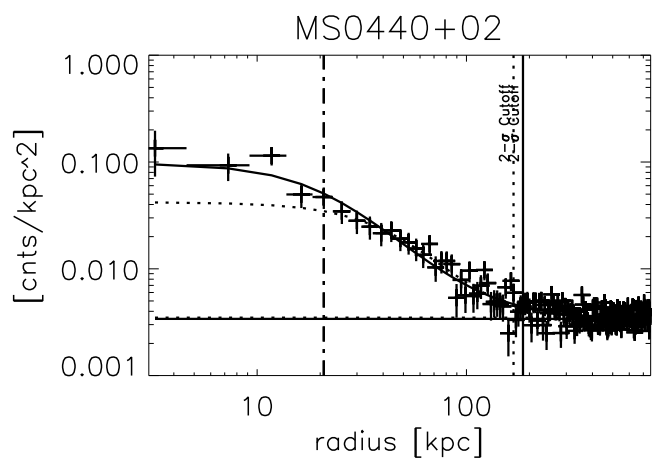
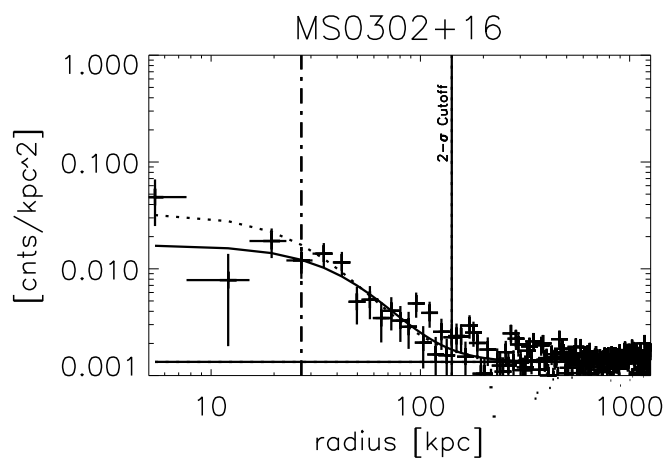
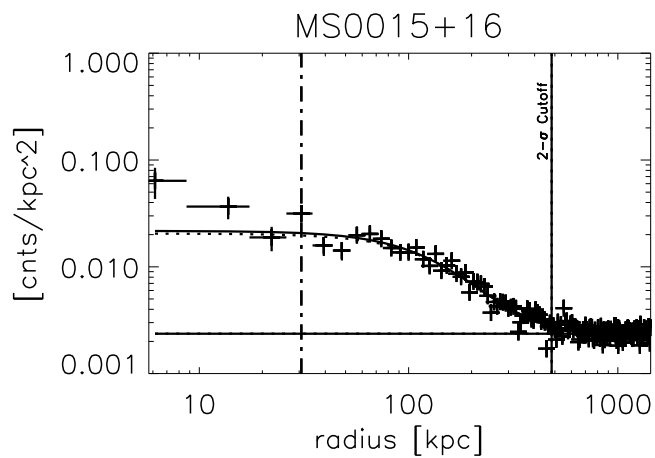
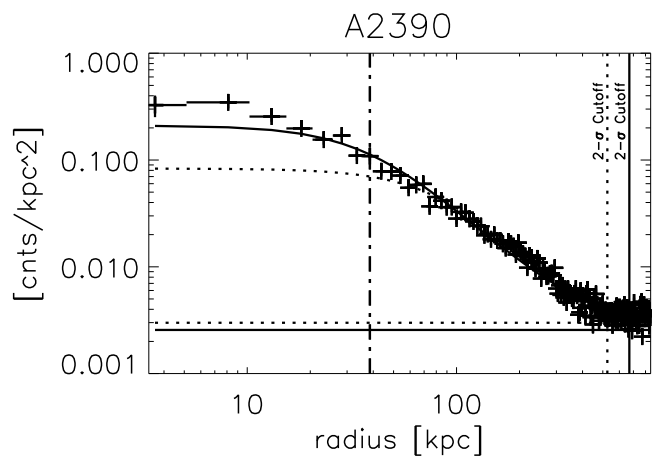
^cThe luminosity fraction is calculated at the Inner Cutoff Radius, listed in Table 3.

Note. — The gas mass fraction average is a weighted average. The error on the gas mass fraction average value is the rms standard deviation.

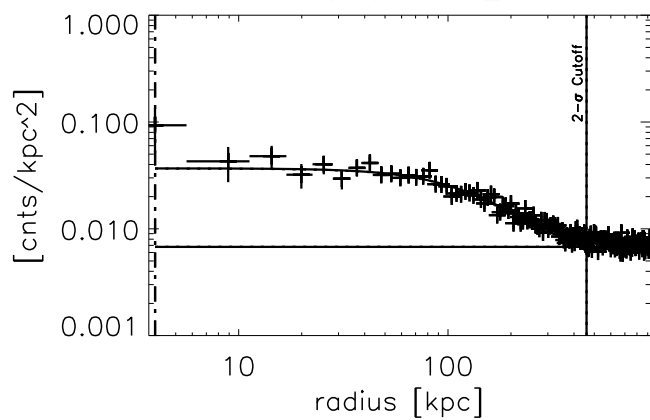




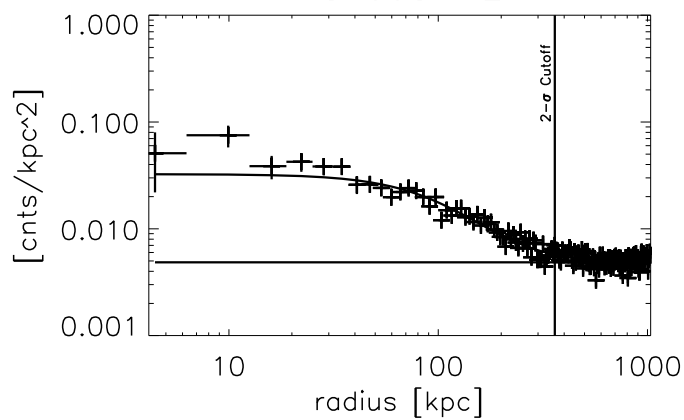




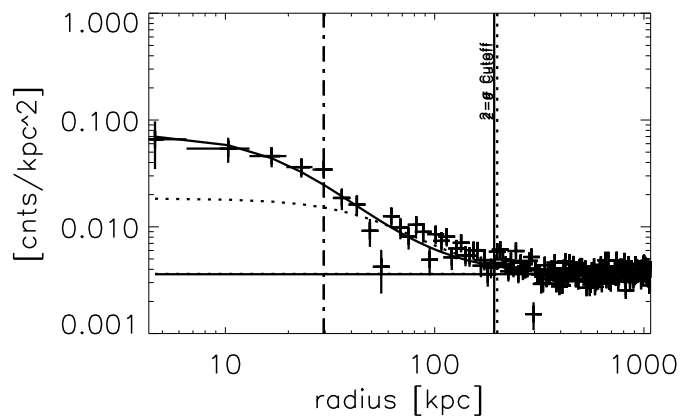
MS1006+12



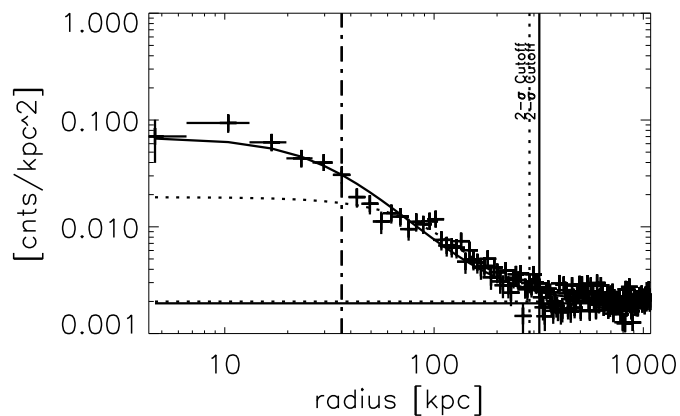
MS1008-12



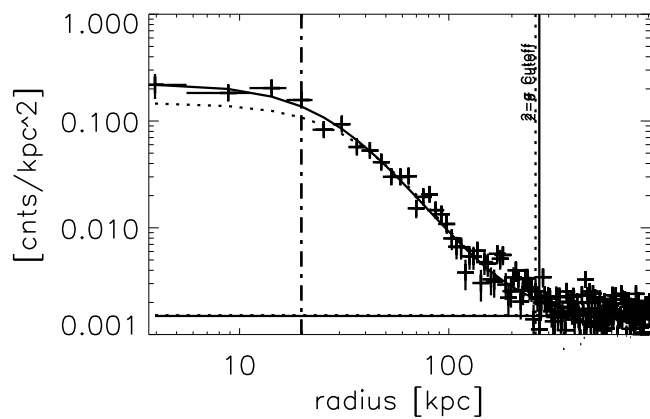
MS1224+20



MS1358+62



MS1455+22



MS1512+36

